

Continuous Symmetry Breaking in a Two-dimensional Rydberg Array

Cheng Chen*,¹ Guillaume Borner*,¹ Marcus Bintz*,² Gabriel Emperauer*,¹ Lucas Leclerc,^{1,3} Vincent S. Liu,² Pascal Scholl,^{1,4} Daniel Barredo,^{1,5} Johannes Hauschild,^{2,6,7} Shubhayu Chatterjee,² Michael Schuler,⁸ Andreas M. Läuchli,^{9,10,8} Michael P. Zaletel,^{2,11} Thierry Lahaye,¹ Norman Y. Yao,^{2,11,12} and Antoine Browaeys¹

¹Université Paris-Saclay, Institut d'Optique Graduate School,
CNRS, Laboratoire Charles Fabry, 91127 Palaiseau Cedex, France

²Department of Physics, University of California, Berkeley, California 94720 USA

³PASQAL SAS, 7 Rue Leonard de Vinci, 91300 Massy, France

⁴California Institute of Technology, Pasadena, CA 91125, USA

⁵Nanomaterials and Nanotechnology Research Center (CINN-CSIC),

Universidad de Oviedo (UO), Principado de Asturias, 33940 El Entrego, Spain

⁶Department of Physics, Technical University of Munich, 85748 Garching, Germany

⁷Munich Center for Quantum Science and Technology (MCQST), Schellingstr. 4, D-80799 München, Germany

⁸Institut für Theoretische Physik, Universität Innsbruck, A-6020 Innsbruck, Austria

⁹Laboratory for Theoretical and Computational Physics, Paul Scherrer Institute, 5232 Villigen, Switzerland

¹⁰Institute of Physics, Ecole Polytechnique Fédérale de Lausanne (EPFL), 1015 Lausanne, Switzerland

¹¹Materials Sciences Division, Lawrence Berkeley National Laboratory, Berkeley, CA 94720, USA

¹²Department of Physics, Harvard University, Cambridge, Massachusetts 02138 USA

(Dated: February 20, 2023)

Spontaneous symmetry breaking underlies much of our classification of phases of matter and their associated transitions [1–3]. The nature of the underlying symmetry being broken determines many of the qualitative properties of the phase; this is illustrated by the case of discrete versus continuous symmetry breaking. Indeed, in contrast to the discrete case, the breaking of a continuous symmetry leads to the emergence of gapless Goldstone modes controlling, for instance, the thermodynamic stability of the ordered phase [4, 5]. Here, we realize a two-dimensional dipolar XY model – which exhibits a continuous spin-rotational symmetry – utilizing a programmable Rydberg quantum simulator. We demonstrate the adiabatic preparation of correlated low-temperature states of both the XY ferromagnet and the XY antiferromagnet. In the ferromagnetic case, we characterize the presence of long-range XY order, a feature prohibited in the absence of long-range dipolar interaction. Our exploration of the many-body physics of XY interactions complements recent works utilizing the Rydberg-blockade mechanism to realize Ising-type interactions exhibiting discrete spin rotation symmetry [6–9].

Constraints on when and how symmetries can be broken in many-particle systems abound. For example, long-wavelength fluctuations preclude the breaking of continuous symmetries in low-dimensional systems with short-range interactions [10–14]. The presence of long-range interactions qualitatively alters this picture [15]. On the one hand, they can stabilize certain forms of finite-temperature order, which would otherwise be forbidden [16–19]. On the other hand, they can also lead to frustration, where interactions compete with one another, preventing the formation of order [20–24]. Even when order persists in both the short- and long-range cases, the nature of this order, including the dispersion of excitations or the decay of correlation functions, can be fundamentally distinct [18, 25–27].

Synthetic quantum systems are ideally suited to study these

features. While ultra-cold atoms in optical lattices have investigated continuous symmetry breaking with contact interaction [28], dipolar molecules in lattices [29–32] or trapped ions [33–36] are promising platforms to realize the long-range case. Here, we use a Rydberg quantum simulator to realize a long-range interacting, two-dimensional XY spin system with either ferromagnetic (FM) or antiferromagnetic (AFM) couplings. We arrange up to $N = 100$ dipolar interacting Rydberg atoms into a defect-free square lattice, so that the many-body ground state in either the FM or AFM case is in a continuous symmetry breaking phase characterized by off-diagonal long-range order [37]. For the dipolar XY FM, theory predicts that this continuous symmetry breaking order persists in the presence of thermal fluctuations [17, 18, 27]. On the contrary, dipolar interactions are insufficient to stabilize finite temperature, long-range order in the antiferromagnet [14]. Rather, one expects power-law decaying, algebraic long-range order due to Berezinskii-Kosterlitz-Thouless physics [38–42].

Our main results are threefold. First, leveraging single-site addressing, we adiabatically prepare correlated low-temperature states of both the XY FM and the XY AFM starting from a classical staggered spin configuration. Second, we characterize the prepared states by measuring the full spatial profile of correlation functions. In the ferromagnet, the system exhibits correlations consistent with the presence of long-range order – a feature prohibited in conventional short-range-interacting, two-dimensional magnets [12, 13]. Meanwhile, in the antiferromagnet, correlations vanish at long distances, consistent with the decay expected from algebraic long-range order. We also show that the states produced are not classical FM or AFM. Third, by introducing a partial quench into the adiabatic ramp, we study the robustness of the magnetic order with respect to an excess energy akin to an effective temperature. This allows us to probe the phase diagram of the dipolar XY model (Fig. 1).

The experimental setup (Fig. 1a) consists of a two-dimensional square lattice of ^{87}Rb atoms trapped in an op-

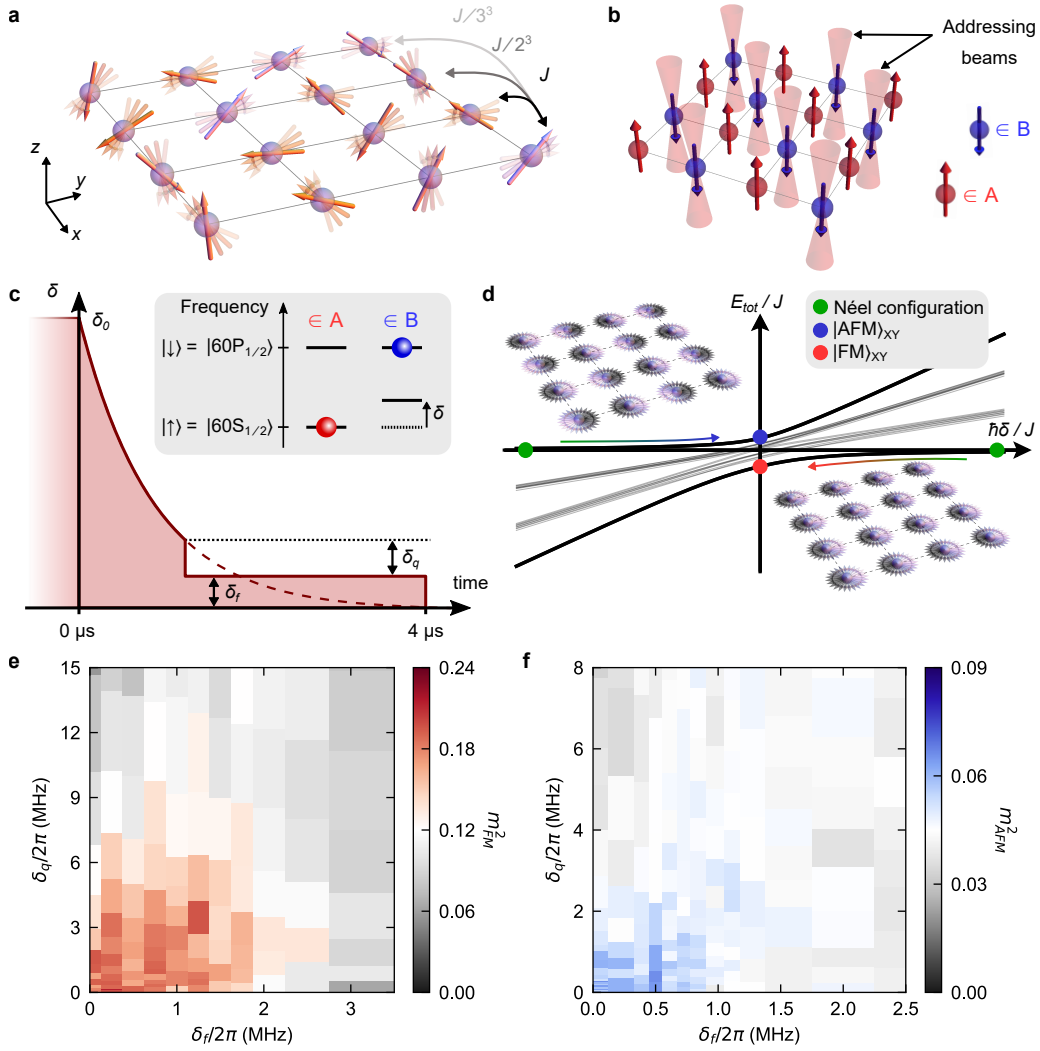


Figure 1. Dipolar XY model in a Rydberg quantum simulator and experimental phase diagram. **a**, Schematic depicting the long-range dipolar XY model. An effective spin is encoded in a pair of Rydberg states which exhibit dipolar flip-flop interactions. **b**, A spatially dependent light-shift is used to prepare the system in a Néel spin configuration. **c**, The amplitude δ of the light-shift is decreased as a function of time to a final value, δ_f . To study the robustness of the magnetic order with respect to an excess energy, we introduce a diabatic quench of magnitude δ_q . **d**, Energy spectrum of H_{tot} as a function of δ , for $N = 2 \times 3$. When starting in the ground state for $\hbar\delta/J \gg 1$, the system is adiabatically ramped to the ferromagnetic XY state, pictured by the colored fluctuating arrows correlated in directions. When starting in the highest excited state for $\hbar\delta/J \ll -1$, the system is adiabatically ramped to the antiferromagnetic XY state, portrayed by the anticorrelated fluctuating arrows. **e**, Ferromagnetic phase diagram depicting the magnetization squared as a function of the final staggered field strength, δ_f and the diabatic quench magnitude, δ_q . Symmetry breaking is expected in a lobe about $(\delta_f = 0, \delta_q = 0)$ and is destroyed by either quantum (δ_f) or thermal (δ_q) fluctuations. On a 6×7 system, a crossover between ordered and disordered behavior is observed. **f**, Analogous phase diagram for the antiferromagnet. Note that at finite temperature, only algebraic long-range order is expected.

tical tweezer array [8]. We encode an effective spin $1/2$ in a pair of opposite-parity Rydberg states, $|\uparrow\rangle = |60S_{1/2}\rangle$ and $|\downarrow\rangle = |60P_{1/2}\rangle$. Resonant dipole-dipole interactions between the spins naturally realize the dipolar XY model [43],

$$H_{\text{XY}} = -\frac{J}{2} \sum_{i < j} \frac{a^3}{r_{ij}^3} (\sigma_i^x \sigma_j^x + \sigma_i^y \sigma_j^y), \quad (1)$$

where σ_i^α are Pauli matrices, r_{ij} is the distance between spins i and j , $J/\hbar = 0.77$ MHz is the dipolar interaction strength,

and $a = 12.5 \mu\text{m}$ is the lattice spacing; here, the quantization axis is defined by an external magnetic field perpendicular to the lattice plane, which ensures that the dipolar interactions are isotropic. The Hamiltonian exhibits a continuous $U(1)$ symmetry corresponding to the conservation of total z -magnetization, $M^z = \sum_i \sigma_i^z$ (see Methods Sec. C 1).

The starting point of our experiments is a classical Néel spin configuration, i.e. a staggered arrangement of spins $|\downarrow\rangle$ and $|\uparrow\rangle$ with $M^z = 0$, prepared in the following way (see Methods Sec. A 2): after initializing all the atoms in $|\uparrow\rangle$,

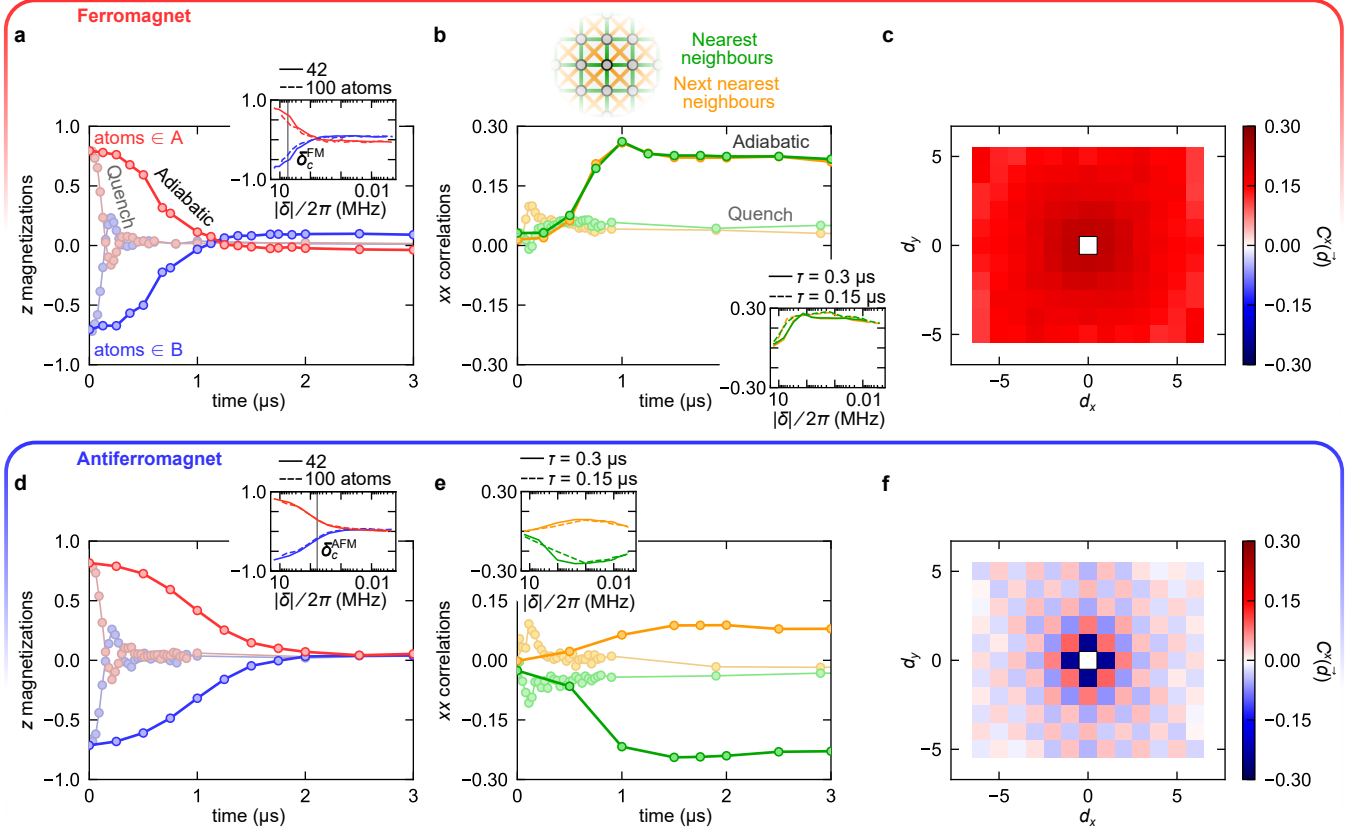


Figure 2. **Adiabatic preparation of dipolar XY ferro- and antiferromagnets.** **a**, Sublattice-resolved magnetization $\langle \sigma_i^z \rangle$ as the staggered field $\delta(t)$ is reduced. At $t = 0$, the state is prepared in a classical Néel state along the z -axis, as indicated by the opposing magnetization of atoms in the A (red) and B (blue) sublattices. As the staggered field $\delta(t)$ is turned off, either adiabatically or via a sudden quench, the Néel magnetization decays towards zero. (inset) Comparison of the z -magnetizations decay as a function of δ for a 6×7 versus a 10×10 lattice. The gray vertical line indicates the value δ_c^{FM} where the phase transition occurs, inferred from the theory (Methods C 2). **b**, The formation of a low-energy XY-ferromagnet is detected via the in-plane two-point correlation function, $C_{i,j}^x$. Data is shown for i, j averaged over either nearest or next-nearest pairs. The sudden quench produces additional energy which destroys the XY order and leads to correlations near zero. (inset) Nearest and next-nearest correlations for two different adiabatic ramp rates. **c**, xx correlations as a function of displacement, $C^x(\vec{d}) \equiv \langle C_{\vec{r}, \vec{r}+\vec{d}}^x \rangle_{\vec{r}}$, measured at time, $t = 2 \mu\text{s}$ (with d_x and d_y in units of lattice spacing a). **d-f**, Analogous results for the antiferromagnetic case. Crucially (**e,f**), we observe staggered correlations.

we apply focused laser beams to produce spatially dependent light-shifts, implementing the Hamiltonian $H_Z = \hbar \delta \sum_i n_i$. The n_i form a staggered pattern with $n_i = 0$ on the A-sublattice and $n_i = (1 + \sigma_i^z)/2$ on the B-sublattice (Fig. 1b). We then sweep a global microwave pulse across the resonance of the atoms in the A-sublattice that flips their spin to $|\downarrow\rangle$. This leads to the Néel configuration, which is a good approximation of the ground state (for $\delta > 0$) or highest excited state (for $\delta < 0$) of the total Hamiltonian $H_{\text{tot}} = H_{\text{XY}} + H_Z$ for $\hbar|\delta| \gg J$.

Starting from this configuration, we dynamically prepare highly-correlated, quantum many-body states by ramping down as a function of time the laser field producing the staggered light-shifts, either abruptly or adiabatically (Fig. 1c) (for a discussion of an alternative preparation approach, see Methods Sec. D 1). In the adiabatic case, for $\delta(t) > 0$, the ramp connects the Néel configuration to the low-temperature ferromagnetic states of H_{XY} , as shown in Fig. 1d. Meanwhile, for

$\delta(t) < 0$, the adiabatic ramp prepares *negative* temperature states of H_{XY} or equivalently, low-temperature antiferromagnetic states of $-H_{\text{XY}}$ (Fig. 1d) [44]. In the thermodynamic limit of both cases, a quantum phase transition is expected to occur at some critical $\delta_c^{\text{FM/AFM}}$, between the Néel configuration and the XY order (Methods C 3).

To investigate the XY ferromagnet, we begin with a 6×7 lattice and utilize an exponential ramp profile, $\delta(t) \approx \delta_0 e^{-t/\tau}$, with $\delta_0 = 2\pi \times 15$ MHz and $\tau = 0.3 \mu\text{s}$. As depicted in Fig. 2a, for both sublattices, the on-site z -magnetization, $2 \sum_{i \in A/B} \langle \sigma_i^z \rangle / N$, obtained by averaging over many realizations of the experiment, decreases toward zero, with a residual late-time offset arising from experimental imperfections (see Methods Sec. B 2). This is consistent with the XY ferromagnet, which orders in the equatorial plane, but by itself, is insufficient to diagnose the phase. Indeed, quenching the staggered light-shifts (in less than 100 ns) leads to a near infinite temperature state, which also exhibits a magnetization

that rapidly relaxes to zero (lighter curves, Fig. 2a).

The key characteristic of the XY ferromagnet is only revealed upon measuring the correlation function, $C_{ij}^x = \langle \sigma_i^x \sigma_j^x \rangle - \langle \sigma_i^x \rangle \langle \sigma_j^x \rangle$ (Methods C 1). For the quenched state, the correlation functions remain near zero for all times, consistent with high-temperature behavior (lighter curves, Fig. 2b). The dynamics of the adiabatic protocol are markedly distinct – both nearest-neighbor and next-nearest-neighbor correlations grow to a stable non-zero value at late times, indicative of order [37]. By switching the sign of δ_0 , we also investigate the XY antiferromagnet. Both the z -magnetization (Fig. 2d) and the correlation functions (Fig. 2e) exhibit qualitatively similar dynamics as the ferromagnetic case. One notable difference is that $C^x < 0$ for nearest-neighbor correlations, indicating that neighboring spins have anti-aligned.

A few remarks are in order. First, to explore the adiabaticity of our protocol, we vary the time-constant of the exponential ramp. As shown in the insets of Fig. 2b,e, the dynamics of the correlation function agree between $\tau = 0.15 \mu\text{s}$ and $\tau = 0.3 \mu\text{s}$, indicating that diabatic errors are not a limiting factor. We confirm this by numerical simulation of the many-body dynamics (see Methods Fig. 11). Second, while the long-range tail of the dipolar interaction reinforces the XY FM order, it is weakly frustrating for the AFM [15]. As a consequence, the phase transition between the Néel configuration and the XY AFM is expected to occur at a smaller value of the staggered light-shift as compared to the XY FM, i.e. $|\delta_c^{\text{AFM}}| < |\delta_c^{\text{FM}}|$ (see also Methods Sec. D). This is indeed borne out by the data where we observe that the magnetization decays to zero faster as a function of δ for the FM case than for the AFM. Third, we increase the system size to a 10×10 lattice and perform the analogous adiabatic preparation protocols. We find the same behavior for all observables (insets, Fig. 2a,d), indicating that our results are robust to finite-size effects [45]. Finally, we observe that at the latest times, the correlations in both the FM and AFM cases exhibit a slow decay; we conjecture that this decay arises from a combination of residual atomic motion and the finite lifetime of the Rydberg states (more details in Methods B 2).

Our measurements of the local correlations suggest we have dynamically prepared low-temperature states of the XY FM and AFM – but are these states truly long-range ordered? To investigate this, we measure the long-distance spin-spin correlations of the system after adiabatic preparation. In Fig. 2c,f [6 \times 7] and Fig. 3a [10 \times 10] we show the correlations as a function of the displacement \vec{d} , averaging over initial positions: $C^x(\vec{d}) \equiv \langle C_{\vec{r}, \vec{r}+\vec{d}}^x \rangle_{\vec{r}}$. The FM correlations are of constant sign and appear to plateau at long distances, indicative of long-range order, while the AFM correlations are staggered and exhibit a decay. For a more quantitative assessment, we focus on the 10×10 array and plot $C^x(d)$, averaging over displacements of the same distance $d = |\vec{d}|$. In the XY AFM, correlations decay to zero at large distances, indicating the absence of long-range order. By contrast, the XY FM indeed exhibits a plateau, $C_\infty^x \sim 0.13$, which establishes it as a magnetically ordered state with an effective magnetization density $m_{\text{eff}} \equiv \sqrt{2C_\infty^x} = 0.51$ (Methods C 1).

For additional insight, in Fig. 3b we compare the measured $C^x(d)$ against the exact ground-state prediction obtained from density matrix renormalization group (DMRG) calculations (see Methods Sec. C 2) [46, 47]. In the DMRG ground state, $C^x(d)$ does plateau in the FM, but slowly decays in the AFM due to finite-size effects – in the thermodynamic limit, both the FM and AFM ground states are expected to be long-range ordered at zero temperature. While the qualitative structure of the measured $C^x(d)$ (e.g. sign structure in the AFM case) is consistent with theory, the experimental correlations are weaker. A number of effects could contribute to this. For example, the finite fidelity of the initial Néel state introduces an entropy density (i.e. an effective finite temperature). This is especially destructive to the AFM, for which finite temperature long-range order is forbidden [14, 15], in agreement with our observation. Other experimental imperfections including readout errors are discussed in the Methods, Sec. B; including these errors in our numerical simulations leads to excellent agreement with the data for the 6×7 lattice (see Methods Fig. 10). However, we also observe that running the adiabatic preparation protocol to longer timescales leads to additional decoherence which adversely affects the ferromagnetic magnetization plateau in a non-trivial fashion; in particular, correlations at the largest distances begin to decay before their shorter-distance counterparts (see Methods B 2).

As a final characterization of the prepared states, we investigate whether each realization of the experiment produces a *classical* magnet pointing in a random direction θ in the xy -plane or a genuinely *quantum* many-body state (see Methods C 1). To do so, we analyze the statistical distribution of M^z , which is conserved during the adiabatic ramp. For a classical FM or AFM, each spin, aligned or anti-aligned along θ , is an equal superposition of $|\uparrow\rangle$ and $|\downarrow\rangle$, so that M^z follows a binomial distribution. By contrast, the ground state of H_{XY} is an eigenstate of M^z , and its variance should be zero. Figure 4a,b shows experimental histograms of the z -magnetization at $t = 2 \mu\text{s}$ for the FM and AFM. Figure 4c presents the variance for various times t . We find that the states have a variance smaller than that of a binomial distribution, indicating that we do not prepare classical magnets. In fact, the measured non-zero variances can be fully explained by the state preparation and measurement errors applied to the ideal distribution (see Methods B 1). We have also checked the rotation invariance of the state around z by measuring the magnetization along y and finding the same as along x . Altogether, our measurements suggest a state which is a coherent quantum superposition over a continuous family of classical configurations (see Methods C 1). For such a state, the defining signature of continuous symmetry breaking order is a long-distance plateau in the correlation function $C^x(d)$ – as we observed in the XY FM [5].

As mentioned earlier, the long-range order observed in the FM case should persist at finite temperature. We therefore investigate the stability of the prepared magnetic orders as a function of an effective temperature. To do so, we insert a partial quench of amplitude δ_q into the ramp, followed by an equilibration time of at least $1 \mu\text{s}$ at a final value δ_f of the staggered field (Fig. 1d): the variable quench introduces ex-

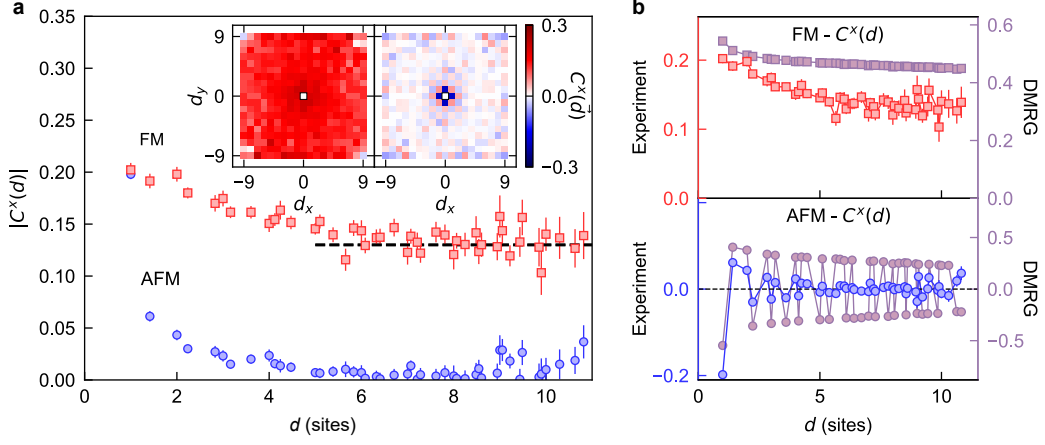


Figure 3. **Observing long-range XY order in a 10×10 lattice.** **a**, xx correlations averaging over displacements of the same distance, $C^x(d)$. The XY ferromagnet exhibits a plateau consistent with long-range order, while the XY antiferromagnet exhibits a decay to zero. (inset) Spatial correlations as a function of displacement, measured at time $t = 1 \mu\text{s}$. **b**, Comparison of the experimental data shown in **a** with the ground-state results obtained from DMRG.

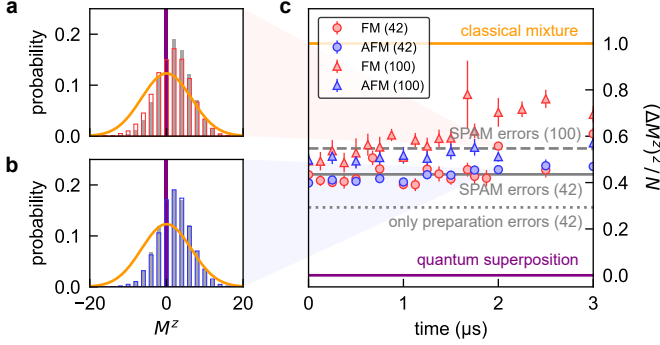


Figure 4. **Analysis of the z -magnetization during the adiabatic ramp.** Experimental histograms of the z -magnetization M^z ($N = 42$) for **a**, the FM and **b**, AFM case together with the ideal case (purple), and the expected distribution including state preparation and measurement errors (grey bars). The orange line is the binomial distribution corresponding to a classical magnet (see text). **c**, normalized variance $(\Delta M^z)^2/N$ as a function of time during the ramp, for the experiment (circles for $N = 42$, triangles for $N = 100$), the classical magnet (orange line) and a perfect XY-magnet (purple line). Grey continuous and dashed lines: ideal case including state preparation and measurement errors. Dotted line: ideal case ($N = 42$) including only state preparation errors.

cess energy into the system, and we observe a relaxation of the magnetization and correlations during the equilibration time. We will use the amplitude of the quench, δ_q , as a proxy for the final effective temperature (see Methods Sec. E). After each $\{\delta_f, \delta_q\}$ ramp, we measure the in-plane magnetization squared, $m_{\text{FM/AFM}}^2 = \sum_{ij} (\pm 1)^{i+j} C_{ij}^x / N^2$ and construct the phase diagram shown in Figs. 1e,f. Starting with the ferromagnet, for small values of δ_f and δ_q (corresponding to low effective temperatures), the magnetization per site is of $\mathcal{O}(1)$, consistent with the ordered phase (Fig. 1e). As either δ_f or δ_q increases, the magnetization density decreases toward zero indicating melting into a disordered phase. This is consis-

tent with theoretical expectations, where δ_q drives the transition via thermal fluctuations [17], while δ_f tunes across the quantum phase transition. We perform the same analysis for the antiferromagnet (Fig. 1f). Compared to the XY ferromagnet, we find that a much smaller region of the $\{\delta_f, \delta_q\}$ phase space exhibits significant AFM correlations, consistent with the frustration induced by the long-range interactions which destabilizes the phase.

Outlook – Looking forward, our work opens the door to a number of future directions. First, it would be interesting to investigate the nature of the phase transition between the disordered and XY-ordered phases; this will require overcoming a number of technical challenges including scaling to larger system sizes. Second, the ability to directly prepare low-temperature states in different M^z magnetization sectors suggests the possibility of directly observing the so-called Anderson tower of states, which underlies continuous symmetry breaking in finite quantum systems [48–51]; the structure of these states has led to recent predictions for scalable spin squeezing by quenching in the ferromagnetic XY phase [52]. Finally, combining optical tweezer geometries which exhibit frustration (i.e. triangular or kagome lattices) with antiferromagnetic interactions leads to a rich landscape for exploring frustrated magnetism and spin liquid physics [20, 22].

ACKNOWLEDGMENTS

We acknowledge the insights of and discussions with M. Aidelburger, L. Henriot, V. Lienhard, J. Moore, C. Laumann, B. Halperin, E. Altman, B. Ye, E. Davis, and M. Block. We are especially indebted to Hans Peter Büchler for insightful comments and discussions about the role of dipolar interactions in the XY model. The computational results presented were performed in part using the FASRC Cannon cluster supported by the FAS Division of Science Research Computing Group at Harvard University, the Savio computational

cluster resource provided by the Berkeley Research Computing program at the University of California, Berkeley and the Vienna Scientific Cluster (VSC). This work is supported by the European Union’s Horizon 2020 research and innovation program under grant agreement No. 817482 (PASQuanS), the Agence Nationale de la Recherche (ANR, project RYBOTIN and ANR-22-PETQ-0004 France 2030, project QuBitAF), and the European Research Council (Advanced grant No. 101018511-ATARAXIA). J.H. acknowledges support from the NSF OIA Convergence Accelerator Program under award number 2040549, and the Munich Quantum Valley, which is supported by the Bavarian state government with funds from the Hightech Agenda Bayern Plus. MS and AML acknowledge support by the Austrian Science Fund (FWF) through Grant No. I 4548. DB acknowledges support from MCIN/AEI/10.13039/501100011033 (RYC2018- 025348-I, PID2020-119667GA-I00, and European Union NextGenerationEU PRTR-C17.I1) M.Z. acknowledges support from the DOE Early Career program and the Alfred P. Sloan foundation. N.Y.Y. acknowledges support from the Army Research Office (W911NF-21-1-0262), the AFOSR MURI program (W911NF-20-1-0136), the David and Lucile Packard foundation, and the Alfred P. Sloan foundation. M.B. and V.L. acknowledge support from NSF QLCI program (grant

no. OMA-2016245). S.C. acknowledges support from the ARO through the MURI program (grant number W911NF-17-1-0323) and from the U.S. DOE, Office of Science, Office of Advanced Scientific Computing Research, under the Accelerated Research in Quantum Computing (ARQC) program.

AUTHOR CONTRIBUTIONS

*CC, GB, MB, and GE contributed equally to this work. CC, GB, GE, PS and DB carried out the experiments. MB, LL, VSL, JH, SC and MS conducted the theoretical analysis and simulations. AML, MPZ, TL, NYY and AB supervised the work. All authors contributed to the data analysis, progression of the project, and on both the experimental and theoretical side. All authors contributed to the writing of the manuscript. Correspondence and requests for materials should be addressed to AB.

ETHICS DECLARATION

AB and TL are co-founders and shareholders of PASQAL.

-
- [1] Landau, L. D. On the theory of phase transitions. I. *Zh. Eksp. Teor. Fiz.* **11**, 19 (1937).
 - [2] Landau, L. D. & Ginzburg, V. L. On the theory of superconductivity. *Zh. Eksp. Teor. Fiz.* **20**, 1064 (1950).
 - [3] Kepler, J. *De Nive Sexangula* (Gottfried Tampach, Frankfurt, 1611).
 - [4] Goldstone, J. Field theories with “Superconductor” solutions. *Il Nuovo Cimento* **19**, 154–164 (1961).
 - [5] Tasaki, H. *Physics and Mathematics of Quantum Many-Body Systems*. Graduate Texts in Physics (Springer International Publishing, Cham, 2020).
 - [6] Schauß, P. *et al.* Crystallization in ising quantum magnets. *Science* **347**, 1455–1458 (2015).
 - [7] Guardado-Sanchez, E. *et al.* Probing the quench dynamics of antiferromagnetic correlations in a 2D quantum Ising spin system. *Phys. Rev. X* **8**, 021069 (2018).
 - [8] Scholl, P. *et al.* Quantum simulation of 2D antiferromagnets with hundreds of Rydberg atoms. *Nature* **595**, 233–238 (2021).
 - [9] Ebadi, S. *et al.* Quantum phases of matter on a 256-atom programmable quantum simulator. *Nature* **595**, 227–232 (2021).
 - [10] Bloch, F. Zur Theorie des Ferromagnetismus. *Zeitschrift für Physik* **61**, 206–219 (1930).
 - [11] Peierls, R. Quelques propriétés typiques des corps solides. *Annales de l’institut Henri Poincaré* **5**, 177–122 (1935).
 - [12] Mermin, N. D. & Wagner, H. Absence of Ferromagnetism or Antiferromagnetism in One- or Two-Dimensional Isotropic Heisenberg Models. *Physical Review Letters* **17**, 1133–1136 (1966).
 - [13] Hohenberg, P. C. Existence of Long-Range Order in One and Two Dimensions. *Physical Review* **158**, 383–386 (1967).
 - [14] Bruno, P. Absence of Spontaneous Magnetic Order at Nonzero Temperature in One- and Two-Dimensional Heisenberg and XY Systems with Long-Range Interactions. *Physical Review Letters* **87**, 137203 (2001).
 - [15] Defenu, N. *et al.* Long-range interacting quantum systems. *arXiv:2109.01063* (2021).
 - [16] Dyson, F. J. Existence of a phase-transition in a one-dimensional Ising ferromagnet. *Communications in Mathematical Physics* **12**, 91–107 (1969).
 - [17] Kunz, H. & Pfister, C. E. First order phase transition in the plane rotator ferromagnetic model in two dimensions. *Communications in Mathematical Physics* **46**, 245–251 (1976).
 - [18] Maleev, S. V. Dipole forces in two-dimensional and layered ferromagnets. *Soviet Journal of Experimental and Theoretical Physics* **43**, 1240 (1976).
 - [19] Fröhlich, J., Israel, R., Lieb, E. H. & Simon, B. Phase transitions and reflection positivity. I. General theory and long range lattice models. *Communications in Mathematical Physics* **62**, 1–34 (1978).
 - [20] Diep, H. T. (ed.) *Frustrated Spin Systems* (World Scientific, New Jersey, 2013), 2nd edition edn.
 - [21] Castelnovo, C., Moessner, R. & Sondhi, S. L. Magnetic monopoles in spin ice. *Nature* **451**, 42–45 (2008).
 - [22] Yao, N. Y., Zaletel, M. P., Stamper-Kurn, D. M. & Vishwanath, A. A quantum dipolar spin liquid. *Nature Physics* **14**, 405–410 (2018).
 - [23] Keleş, A. & Zhao, E. Absence of Long-Range Order in a Triangular Spin System with Dipolar Interactions. *Physical Review Letters* **120**, 187202 (2018).
 - [24] Keleş, A. & Zhao, E. Renormalization group analysis of dipolar Heisenberg model on square lattice. *Physical Review B* **97**, 245105 (2018).
 - [25] De’Bell, K., MacIsaac, A. B. & Whitehead, J. P. Dipolar effects in magnetic thin films and quasi-two-dimensional systems. *Rev. Mod. Phys.* **72**, 225–257 (2000).

- [26] Taroni, A., Bramwell, S. T. & Holdsworth, P. C. W. Universal window for two-dimensional critical exponents. *Journal of Physics: Condensed Matter* **20**, 275233 (2008).
- [27] Peter, D., Müller, S., Wessel, S. & Büchler, H. P. Anomalous behavior of spin systems with dipolar interactions. *Physical Review Letters* **109**, 025303 (2012).
- [28] Mazurenko, A. *et al.* A cold-atom Fermi-Hubbard antiferromagnet. *Nature* **545**, 462 (2017).
- [29] Yan, B. *et al.* Observation of dipolar spin-exchange interactions with lattice-confined polar molecules. *Nature* **501**, 521–525 (2013).
- [30] Christakis, L. *et al.* Probing site-resolved correlations in a spin system of ultracold molecules. *arXiv:2207.09328* (2022).
- [31] Chomaz, L. *et al.* Dipolar physics: A review of experiments with magnetic quantum gases. *arXiv:2201.02672* (2022).
- [32] Leo, N. *et al.* Collective magnetism in an artificial 2D XY spin system. *Nature Communications* **9**, 2850 (2018).
- [33] Richerme, P. *et al.* Non-local propagation of correlations in quantum systems with long-range interactions. *Nature* **511**, 198–201 (2014).
- [34] Jurcevic, P. *et al.* Quasiparticle engineering and entanglement propagation in a quantum many-body system. *Nature* **511**, 202–205 (2014).
- [35] Maghrebi, M. F., Gong, Z.-X. & Gorshkov, A. V. Continuous symmetry breaking in 1d long-range interacting quantum systems. *Phys. Rev. Lett.* **119**, 023001 (2017).
- [36] Feng, L. *et al.* Continuous symmetry breaking in a trapped-ion spin chain. *arXiv:2211.01275* (2022).
- [37] Yang, C. N. Concept of off-diagonal long-range order and the quantum phases of liquid He and of superconductors. *Reviews of Modern Physics* **34**, 694–704 (1962).
- [38] Berezinskii, V. L. Destruction of Long-range Order in One-dimensional and Two-dimensional Systems having a Continuous Symmetry Group I. Classical Systems. *Soviet Journal of Experimental and Theoretical Physics* **32**, 493 (1971).
- [39] Berezinskii, V. L. Destruction of Long-range Order in One-dimensional and Two-dimensional Systems Possessing a Continuous Symmetry Group. II. Quantum Systems. *Soviet Journal of Experimental and Theoretical Physics* **34**, 610 (1972).
- [40] Kosterlitz, J. M. & Thouless, D. J. Ordering, metastability and phase transitions in two-dimensional systems. *Journal of Physics C: Solid State Physics* **6**, 1181–1203 (1973).
- [41] Kosterlitz, J. M. The critical properties of the two-dimensional XY model. *Journal of Physics C: Solid State Physics* **7**, 1046–1060 (1974).
- [42] Giachetti, G., Defenu, N., Ruffo, S. & Trombettoni, A. Berezinskii-Kosterlitz-Thouless Phase Transitions with Long-Range Couplings. *Physical Review Letters* **127**, 156801 (2021).
- [43] Browaeys, A. & Lahaye, T. Many-body physics with individually controlled Rydberg atoms. *Nature Physics* **16**, 132 (2020).
- [44] Sørensen, A. S. *et al.* Adiabatic preparation of many-body states in optical lattices. *Physical Review A* **81**, 061603 (2010).
- [45] Sandvik, A. W. & Hamer, C. J. Ground-state parameters, finite-size scaling, and low-temperature properties of the two-dimensional $S = 1/2$ XY model. *Physical Review B* **60**, 6588–6593 (1999).
- [46] White, S. R. Density matrix formulation for quantum renormalization groups. *Physical Review Letters* **69**, 2863–2866 (1992).
- [47] Hauschild, J. & Pollmann, F. Efficient numerical simulations with Tensor Networks: Tensor Network Python (TeNPy). *SciPost Physics Lecture Notes* **5** (2018).
- [48] Anderson, P. W. An Approximate Quantum Theory of the Antiferromagnetic Ground State. *Physical Review* **86**, 694–701 (1952).
- [49] Anderson, P. W. *Basic Notions of Condensed Matter Physics*. Advanced Book Classics (Perseus Publ, Cambridge, Mass, 2010), 10. pr edn.
- [50] Tasaki, H. Long-Range Order, “Tower” of States, and Symmetry Breaking in Lattice Quantum Systems. *Journal of Statistical Physics* **174**, 735–761 (2019).
- [51] Beekman, A., Rademaker, L. & van Wezel, J. An introduction to spontaneous symmetry breaking. *SciPost Physics Lecture Notes* **11** (2019).
- [52] Comparin, T., Mezzacapo, F. & Roscilde, T. Robust spin squeezing from the tower of states of U(1)-symmetric spin Hamiltonians. *Physical Review A* **105**, 022625 (2022).
- [53] Barredo, D., de Léséleuc, S., Lienhard, V., Lahaye, T. & Browaeys, A. An atom-by-atom assembler of defect-free arbitrary 2d atomic arrays. *Science* **354**, 1021–1023 (2016).
- [54] de Léséleuc, S., Barredo, D., Lienhard, V., Browaeys, A. & Lahaye, T. Analysis of imperfections in the coherent optical excitation of single atoms to Rydberg states. *Physical Review A* **97**, 053803 (2018).
- [55] Kennedy, T., Lieb, E. H. & Shastry, B. S. The XY Model Has Long-Range Order for All Spins and All Dimensions Greater than One. In Nachtergaele, B., Solovej, J. P. & Yngvason, J. (eds.) *Statistical Mechanics*, 327–329 (Springer Berlin Heidelberg, Berlin, Heidelberg, 1988).
- [56] Björnberg, J. E. & Ueltschi, D. Reflection positivity and infrared bounds for quantum spin systems. *arXiv:2204.12896* (2022).
- [57] In preparation.
- [58] Stoudenmire, E. & White, S. R. Studying Two-Dimensional Systems with the Density Matrix Renormalization Group. *Annual Review of Condensed Matter Physics* **3**, 111–128 (2012).
- [59] Hastings, M. B. & Koma, T. Spectral Gap and Exponential Decay of Correlations. *Communications in Mathematical Physics* **265**, 781–804 (2006).
- [60] Lienhard, V. *et al.* Observing the space- and time-dependent growth of correlations in dynamically tuned synthetic Ising antiferromagnets. *Physical Review X* **8**, 021070 (2018).
- [61] de Léséleuc, S. *et al.* Observation of a symmetry-protected topological phase of interacting bosons with Rydberg atoms. *Science* **365**, 775–780 (2019).
- [62] Jensen, P. J., Bennemann, K. H., Morr, D. K. & Dreyssé, H. Two-dimensional Heisenberg antiferromagnet in a transverse field. *Physical Review B* **73**, 144405 (2006).
- [63] Kar, S., Wierschem, K. & Sengupta, P. Magnons in a two-dimensional transverse-field XXZ model. *Physical Review B* **96**, 045126 (2017).
- [64] Gu, S.-J. Fidelity approach to quantum phase transitions. *International Journal of Modern Physics B* **24**, 4371–4458 (2010).
- [65] Zaletel, M. P., Mong, R. S. K., Karrasch, C., Moore, J. E. & Pollmann, F. Time-evolving a matrix product state with long-ranged interactions. *Physical Review B* **91**, 165112 (2015).
- [66] Mermin, N. D. Crystalline order in two dimensions. *Physical Review* **176**, 250–254 (1968).
- [67] Fröhlich, J. & Pfister, C. On the absence of spontaneous symmetry breaking and of crystalline ordering in two-dimensional systems. *Communications in Mathematical Physics* **81**, 277–298 (1981).
- [68] Tobochnik, J. & Chester, G. V. Monte Carlo study of the planar spin model. *Physical Review B* **20**, 3761–3769 (1979).
- [69] Ueda, A. & Oshikawa, M. Resolving the Berezinskii-Kosterlitz-Thouless transition in the two-dimensional XY model with tensor-network-based level spectroscopy. *Physical Review B* **104**, 165132 (2021).

- [70] Ding, H.-Q. & Makivić, M. S. Kosterlitz-Thouless transition in the two-dimensional quantum XY model. *Physical Review B* **42**, 6827–6830 (1990).
- [71] Ding, H.-Q. Phase transition and thermodynamics of quantum XY model in two dimensions. *Physical Review B* **45**, 230–242 (1992).
- [72] Romano, S. Computer simulation study of a long-range plane-rotator system in two dimensions. *Nuovo Cim, B* **100**, 447–466 (1987).
- [73] Romano, S. Computer-simulation study of a disordered plane-rotator system in two dimensions with long-range ferromagnetic interactions. *Physical Review B* **42**, 8647–8650 (1990).
- [74] Fisher, M. E., Ma, S.-k. & Nickel, B. G. Critical Exponents for Long-Range Interactions. *Physical Review Letters* **29**, 917–920 (1972).
- [75] Sak, J. Recursion Relations and Fixed Points for Ferromagnets with Long-Range Interactions. *Physical Review B* **8**, 281–285 (1973).
- [76] Stoudenmire, E. M. & White, S. R. Minimally entangled typical thermal state algorithms. *New Journal of Physics* **12**, 055026 (2010).
- [77] Binder, M. & Barthel, T. Symmetric minimally entangled typical thermal states for canonical and grand-canonical ensembles. *Physical Review B* **95**, 195148 (2017).
- [78] Gubernatis, J., Kawashima, N. & Werner, P. *Quantum Monte Carlo Methods: Algorithms for Lattice Models* (Cambridge University Press, 2016), first edn.
- [79] Syljuasen, O. F. & Sandvik, A. W. Quantum Monte Carlo with directed loops. *Physical Review E* **66**, 046701 (2002).
- [80] Calabrese, P. & Cardy, J. Time Dependence of Correlation Functions Following a Quantum Quench. *Physical Review Letters* **96**, 136801 (2006).

METHODS

A. Experimental methods

The realization of the dipolar XY model relies on our ^{87}Rb Rydberg-atom tweezer array setup, described in previous works [8, 53]. The pseudo-spin states are $|\uparrow\rangle = |60S_{1/2}, m_J = 1/2\rangle$ and $|\downarrow\rangle = |60P_{1/2}, m_J = -1/2\rangle$. We manipulate them using resonant microwaves at 16.7 GHz. A ~ 50 -G magnetic field, perpendicular to the array, defines the quantization axis (Fig. 5a) and shifts away the irrelevant Zeeman states of the $60S_{1/2}$ and $60P_{1/2}$ manifolds.

1. Addressability in the tweezer array

The addressing laser pattern used to prepare the initial classical Néel configuration is generated by a 1013-nm laser beam detuned from the transition between the intermediate state $6P_{3/2}$ and $|\uparrow\rangle$ (Fig. 5b). The sign of the detuning sets the one of the light-shift: in the FM (resp. AFM) case, the frequency of the addressing laser is tuned below (resp. above) the resonance by ~ 250 MHz.

We use a dedicated spatial light modulator to produce the pattern of addressing beams. Each beam is focused on a $1/e^2$ radius of about $1.5 \mu\text{m}$, for a typical power of 60 mW. We measure the light-shift for each addressed atom by microwave spectroscopy on the $|\uparrow\rangle - |\downarrow\rangle$ transition. The average light-shift is $|\delta_0| = 2\pi \times 15$ MHz over the 42-atom array (21 addressed atoms), and $|\delta_0| = 2\pi \times 9$ MHz over the 100-atom array (50 addressed atoms). These values are dictated by available laser power. For both arrays, the rms dispersion of δ_0 across the addressing beams is 2.4%.

2. Experimental sequence

The experimental sequence is shown in Fig. 5. After assembling the array [53] we use Raman sideband cooling along the radial directions of the tweezers, and reach a temperature of $10 \mu\text{K}$. We then optically pump the atoms in $|g\rangle = |5S_{1/2}, F = 2, m_F = 2\rangle$ before adiabatically ramping down the tweezer depth by a factor ~ 40 . Following this, we switch off the tweezers, and excite the atoms to $|\uparrow\rangle$ using a two-photon stimulated Raman adiabatic passage (STIRAP) with 421-nm and 1013-nm lasers ($\sim 2 \mu\text{s}$ duration).

To generate the classical Néel configuration along z , we first transfer all the atoms from $|\uparrow\rangle$ to $|\downarrow\rangle$ using a 54 ns microwave π -pulse. Subsequently, the addressing beams are applied to the atoms in sublattice B. We then transfer the atoms A from $|\downarrow\rangle$ back to $|\uparrow\rangle$ by an adiabatic microwave sweep while the atoms B remain in $|\downarrow\rangle$, as illustrated in Fig. 5b. In this procedure, exciting first the atoms in $|\downarrow\rangle$ has the advantage of minimizing the depumping of the $|\uparrow\rangle$ atoms by the addressing light (see Sec. B 2 below). An example of perfect Néel configuration obtained at the end of the preparation is shown in Fig. 5c.

The experimental sequence (including the detection part detailed in the next Section) is repeated typically over 1000 defect-free assembled arrays. This allows us to calculate the magnetization and the spin correlations by averaging over these realizations.

3. State detection procedure

At the end of the sequence, we read out the state of each atom in the natural z -basis. To do so, we deexcite the atoms from $|\uparrow\rangle$ to the $5S_{1/2}$ manifold where they are recaptured in the tweezers and imaged. Thus, the $|\uparrow\rangle$ (resp. $|\downarrow\rangle$) state is mapped to the presence (resp. absence) of the corresponding atom. In order to avoid the detrimental effects of the $|\uparrow\rangle - |\downarrow\rangle$ interaction-induced dynamics during the deexcitation, we freeze out the system by shelving the $|\downarrow\rangle$ atoms to $|D\rangle = |59D_{3/2}, m_J = -1/2\rangle$ where they hardly interact with the ones in $|\uparrow\rangle$. This is achieved by using a 48 ns microwave π -pulse at 10.6 GHz. The subsequent deexcitation is performed by applying a $2.5 \mu\text{s}$ light pulse resonant with the transition between $|\uparrow\rangle$ and the short-lived intermediate state $6P_{3/2}$ from which the atoms decay back to $5S_{1/2}$. Additionally, when we want to measure the spins along x we rotate them by applying a 27 ns microwave $\pi/2$ -pulse on the $|\uparrow\rangle - |\downarrow\rangle$ transition prior to the detection. However, this procedure is efficient only for light-shifts $|\delta(t)|$ much smaller than the microwave Rabi frequency, i.e. for times larger than $\sim 0.5 \mu\text{s}$ during an adiabatic preparation.

B. Experimental imperfections

The sequences described above are affected by experimental imperfections. As taking all of them into account is intractable, we estimate here the effect of the main imperfections on the quantities we measure. We first analyse the state preparation and measurement (SPAM) errors and then discuss decoherence in the system.

1. SPAM errors

In order to estimate the SPAM errors, we break down the sequence into a series of steps i , each having a small but finite failure probability η_i . In the following, we keep only the contributions of imperfections to first order in the η_i 's.

As an example, we show in Fig. 6 the discretized sequence corresponding to the preparation and measurement of the classical Néel configuration (corresponding to the time $t = 0$ in Fig. 2a of the main text). Table I gives the corresponding values of the probabilities η_i for 42 atoms, that are either inferred from a series of dedicated experiments, or estimated from numerical simulations. The table also mentions the physical origin of these imperfections.

For atoms in sublattice A (non-addressed), the error tree leads to the probability to recapture the atoms at the end of the sequence, which reads (to first order):

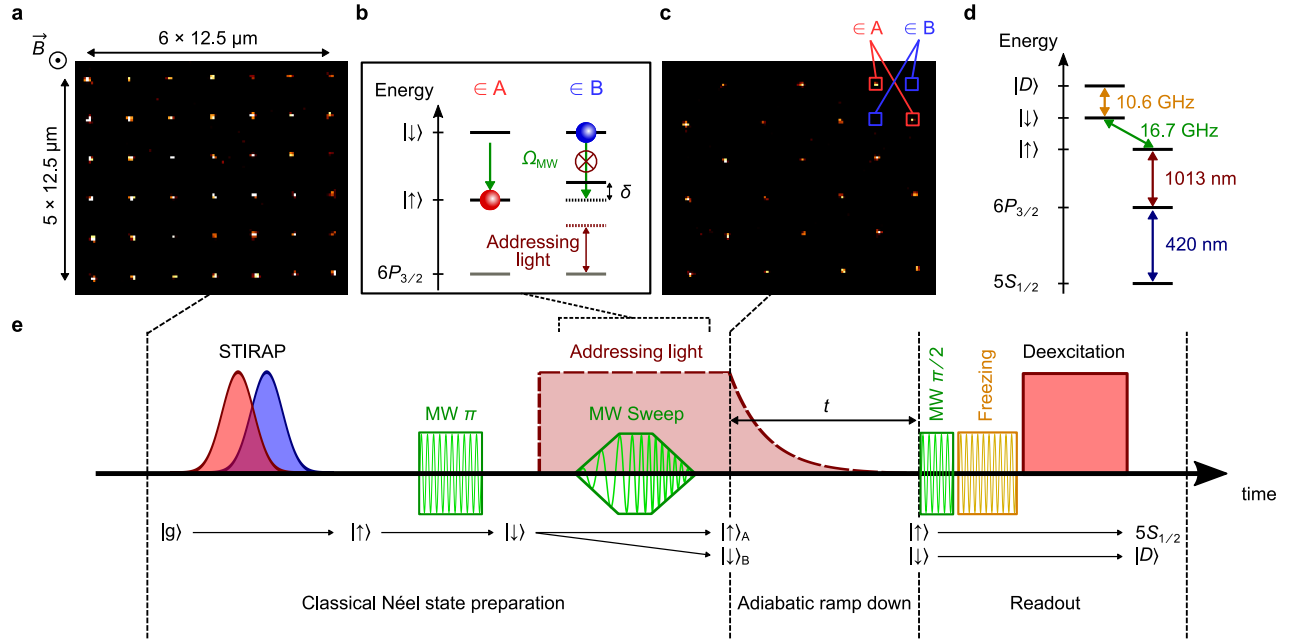


Figure 5. **Experimental procedures and sequence.** **a**, Fluorescence image of the atoms in a fully assembled 6×7 array. **b**, Scheme for the preparation of the initial staggered state. **c**, Detected staggered state, corresponding to the situation for which all the atoms in sublattice A are in $|\uparrow\rangle$, and all the atoms in sublattice B are in $|\downarrow\rangle$. **d**, Schematics of the atomic level diagram. **e**, Experimental sequence.

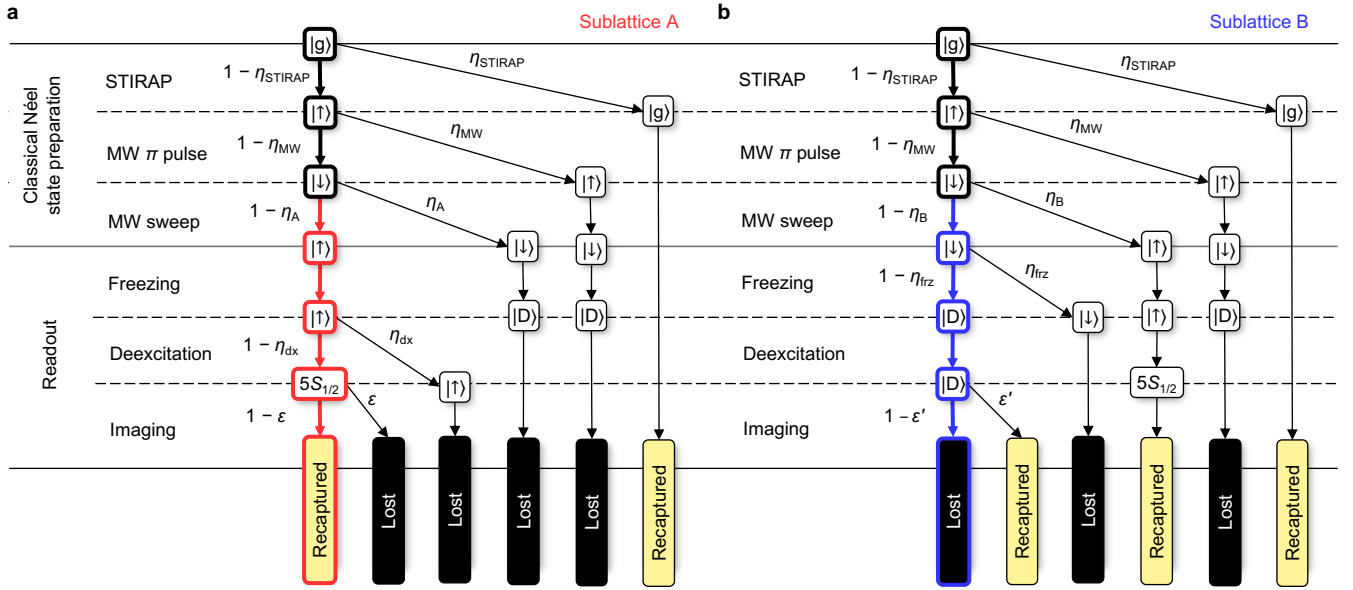


Figure 6. **Simplified error tree associated to the preparation of the initial Néel state**, for **a** the atoms in sublattice A (non-addressed), and **b** in sublattice B (addressed). For simplicity, the events with a probability of order 2 or higher in the η_i , ϵ , ϵ' are disregarded.

$$P_z^A \approx 1 - \eta_{\text{MW}} - \eta_A - \eta_{\text{dx}} - \epsilon. \quad (2)$$

Similarly, the calculation for sublattice B (addressed atoms) yields:

$$P_z^B \approx \eta_{\text{STIRAP}} + \eta_B + \epsilon'. \quad (3)$$

Using the values reported in Table I, we obtain $P_z^A = 0.90$, $P_z^B = 0.15$. From these probabilities, we compute an initial magnetization along z , $\sigma_z^A = 2P_z^A - 1 = 0.8$ and $\sigma_z^B = 2P_z^B - 1 = -0.70$. We checked that these values agree with measured magnetizations at $t = 0$, which are used as a calibration of the errors, for both the FM and the AFM (Fig. 2a,d). Finally the error tree allows us to infer the probability of successful initial preparation per spin. We find 0.87

Stage	Step	Symbol	Value	Main physical origin
Classical Néel state preparation	Rydberg excitation	η_{STIRAP}	5%	Imperfect optical pumping, Laser phase noise, Spontaneous emission from $6P_{3/2}$ [54]
	MW π - pulse	η_{MW}	2%	Effect of H_{XY} during pulse
	MW sweep	η_A, η_B	4%, 5%	Effect of H_{XY} and finite value of $ \delta_0 $
Readout	Freezing	η_{frz}	< 1%	Effect of H_{XY} during pulse
	Deexcitation	η_{dx}	3%	Mechanical effect of deexcitation laser beam
	False $ \downarrow\rangle$	ϵ	1%	Background gas collisions [54]
	False $ \uparrow\rangle$	ϵ'	5%	Rydberg state radiative lifetime [54]

Table I. Summary of the experimental errors defined in Fig. 6, together with their main physical origin.

for the atoms in sublattice A and 0.92 for the ones in B. Using the preparation part of the error tree (Fig. 6), we find $1 - \eta_{\text{STIRAP}} - \eta_{\text{MW}} - \eta_A = 0.89$ for the atoms in sublattice A and $1 - \eta_{\text{STIRAP}} - \eta_{\text{MW}} - \eta_B = 0.88$ for the ones in B. These values are very similar to the ones including detection errors, indicating that this experiment is dominated by preparation errors.

2. Decoherence during the adiabatic ramp

Besides the SPAM errors described previously, additional imperfections lead to decoherence.

First, we focus on the long-time behaviour of the magnetizations for the 10×10 arrays. In Fig. 2a, one observes that, in the FM case, the z -magnetizations of sublattices A and B do not vanish at late times, but reach a constant finite value of a few percent. In contrast, this does not occur in the AFM case (Fig. 2d). We qualitatively explain this effect by the following observations. First, due to off-resonant scattering by the addressing beam, atoms in $|\uparrow\rangle$ are slowly depumped to the ground state $|g\rangle$; we have measured the effective lifetime of an addressed $|\uparrow\rangle$ atom to be $\sim 4 \mu\text{s}$, whether the light-shift is $2\pi \times 15$ or $-2\pi \times 15$ MHz (so that this alone, cannot explain the difference between the FM and AFM cases). However, during our adiabatic ramp down of light-shift $\delta(t)$, the addressed atoms are initially in $|\downarrow\rangle$ (and thus cannot be depumped). Depumping sets in only when the system enters the ordered phase, where an addressed atom has a significant probability to be in $|\uparrow\rangle$. Since $\delta_c^{\text{AFM}} < \delta_c^{\text{FM}}$, the addressing beam intensity (and thus the depumping rate) is at this stage much smaller for the AFM case than for the FM case, and thus has a negligible effect in the former case.

Second, we investigate the role of decoherence on the appearance of long-range order along x in the FM case, for the 10×10 array. Figure 7a shows the time evolution of the nearest-neighbour correlations as we ramp down the light-shift, all the way up to $8 \mu\text{s}$ (in contrast with Fig. 2b of the main text where the evolution is shown only up to $3 \mu\text{s}$, and for 42 atoms). Two timescales appear: first, correlations build

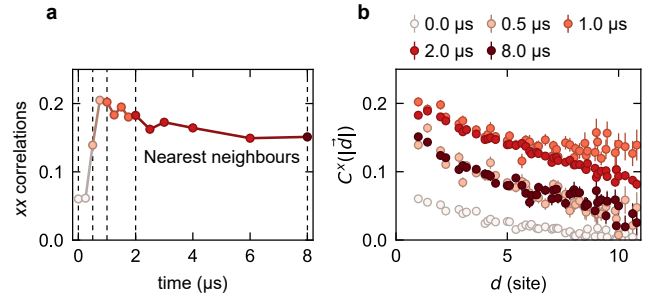


Figure 7. Time dependence of the correlations along x in the FM case for a 10×10 lattice. **a**, Time evolution of the nearest-neighbour correlations along x (different colors correspond to different times). **b**, Spatial correlations as a function of distance, measured at different times $t = \{0.0, 0.5, 1.0, 2.0, 8.0\} \mu\text{s}$ indicated by dashed lines in **a**.

up until $t \simeq 1 \mu\text{s}$ as the FM state is adiabatically prepared; then, they slowly decay and lose 25 % of their value in $7 \mu\text{s}$. This decay is not expected, since the system should be ideally in steady state once it has reached the ferromagnetic phase. We conjecture that the experimental system is affected by decoherence arising from a combination of the residual atomic motion and spontaneous emission from the Rydberg states.

To further analyse the evolution of the ferromagnetic order, we probe the full spatial structure of the correlations at different times. Figure 7b summarizes the results. We observe that for a given distance d all the correlations feature a similar time evolution: a fast increase followed by a slow decay, with a turning point around $1 \mu\text{s}$. For this particular point, the data reveal a plateau for distances of more than 6 sites – the signature of the long range order mentioned in the main text – that disappears for $t \gtrsim 2 \mu\text{s}$. This suggests that despite the decoherence present in the system, we are able to observe the long range ordering expected from the dipolar interactions over a substantial time window.

C. Ground state properties of the XY model

We study here the ground states of the Hamiltonians H_{XY} and $H_{XY} + H_Z$. We define them as in the main text. First:

$$H_{XY} = -\frac{J}{2} \sum_{i < j} \frac{a^3}{r_{ij}^3} [\sigma_i^x \sigma_j^x + \sigma_i^y \sigma_j^y] \quad (4)$$

$$= -\frac{J}{\hbar^2} \sum_{i < j} \frac{a^3}{r_{ij}^3} [S_i^+ S_j^- + S_j^+ S_i^-] \quad (5)$$

where $S_i^\pm = S_i^x \pm i S_i^y = \hbar(\sigma_i^x \pm i \sigma_i^y)/2$ are the ladder operators for spin-1/2 degrees of freedom on a square lattice with N sites, r_{ij} is the distance between sites i, j and a is the lattice spacing. Second, the on-site Hamiltonian is:

$$H_Z = \hbar \delta \sum_{i \in B} \frac{\sigma_i^z + 1}{2} \quad (6)$$

where the magnitude of the light-shift δ depends on the intensity of the addressing laser.

The experimental implementation has a ferromagnetic coupling, $J/\hbar = 0.77$ MHz, and to study antiferromagnetism one must prepare negative temperature states. For theoretical purposes, however, we treat J as a free parameter and frame the discussion in terms of the ground state physics of H_{XY} with either ferromagnetic ($J > 0$) or antiferromagnetic ($J < 0$) coupling. We refer to them as H_{XY}^{FM} and H_{XY}^{AFM} .

It is natural to compare the dipolar H_{XY} to the nearest-neighbor XY model on the square lattice,

$$H_{\text{nn}} = -\frac{J}{2} \sum_{\langle ij \rangle} \sigma_i^x \sigma_j^x + \sigma_i^y \sigma_j^y, \quad (7)$$

where $\langle ij \rangle$ are pairs of neighboring sites, with $i < j$. For H_{nn} , the sign of the coupling J is unimportant, as $U_A H_{\text{nn}} U_A^\dagger = -H_{\text{nn}}$, with $U_A = \prod_{j \in A} e^{-i\pi S_j^z}$. In 1988, Kennedy, Lieb, and Shastry rigorously proved that the unique ground state of H_{nn} has long-range XY order (LRO) [55].

For models with long-range interactions, there are analogous mathematical theorems for classical systems at finite temperature, and for quantum systems in which the interaction strength depends on the Manhattan distance $\|r_i - r_j\|_1$ [19]. In a recent work, Björnberg and Ueltschi addressed quantum spin- S models with interactions depending on the Euclidean distance $\|r_i - r_j\|_2$, although their results require large S and spatial dimension three or higher [56]. Absent a rigorous proof of LRO for the two-dimensional, spin-1/2, dipolar XY model, one can study it using semi-analytic spin wave theory and various numerical methods [18, 22, 27]. In a companion paper [57], we investigate the ground-states of H_{XY} on various geometries, such as tori and infinite cylinders, with an eye towards the thermodynamic limit, $N \rightarrow \infty$. Here, we restrict our focus to finite rectangular arrays as probed in the experiment, and use H_{nn} as a reliable benchmark for comparison.

1. Symmetries, magnetization sectors, and order

As emphasized in the main text, H_{XY} possesses the continuous symmetry: $U_z(\theta) H_{XY} U_z(-\theta) = H_{XY}$ with

$$U_z(\theta) = \exp(-i \sum_j \theta S_j^z / \hbar) = \exp(-i \theta M^z / 2) \quad (8)$$

This operator is generated by the total magnetization, $M^z = \sum_i \sigma_i^z$, and represents the Lie group $U(1) \cong SO(2)$. Additionally, H_{XY} is invariant under the \mathbb{Z}_2 Ising symmetry, $\alpha_2 : (\sigma^x, \sigma^y, \sigma^z) \rightarrow (\sigma^x, -\sigma^y, -\sigma^z)$, as well as any spatial symmetries of the lattice, such as translation or rotation. This model is also time-reversal-symmetric, as represented by the anti-unitary operator $\mathcal{T} = \mathcal{C}$, where \mathcal{C} applies complex conjugation. Here \mathcal{T} differs from the usual $SU(2)$ time-reversal symmetry, which applies the unitary spin rotation $U_y(\pi) = \exp(-i\pi M^y/2)$ in addition to \mathcal{C} . Our atypical choice of $\mathcal{T} = \mathcal{C}$ allows it to remain a symmetry in the presence of the on-site perturbation, H_Z .

In a finite, closed quantum system, all eigenstates $|\psi_n\rangle$ of H_{XY} can be chosen to be simultaneous eigenstates of all of these symmetry operators. In particular, they are eigenstates of the total magnetization, $M^z |\psi_n\rangle = \lambda_n^z |\psi_n\rangle$, and so can be collected into magnetization sectors, conventionally labeled by $S^z = M^z/2$. As a consequence, all M^z -non-conserving operators such as σ_i^x and σ_i^y have identically vanishing expectation values, $\langle \sigma_i^x \rangle = \langle \sigma_i^y \rangle = 0$, in any energy eigenstate $|\psi_n\rangle$, or in any superposition of eigenstates within the same magnetization sector.

In the experiment, systematic errors in the measurement process lead to a small, nonzero $\langle \sigma_i^x \rangle \neq 0$. This value is not a consequence of the physics we are interested in. When analyzing the experimental data, we thus choose to nullify any single-spin contributions by using the *connected* correlator,

$$C^x(i, j) = \langle \sigma_i^x \sigma_j^x \rangle - \langle \sigma_i^x \rangle \langle \sigma_j^x \rangle \quad (9)$$

In the special case of M^z eigenstates with $\langle \sigma^x \rangle = 0$, $C^x(i, j) = \langle \sigma_i^x \sigma_j^x \rangle$. This correlation function is not generically zero. If $|C^x(i, j)|$ approaches a constant $C_\infty^x > 0$ for distantly separated spins i, j , then the corresponding state is said to possess *long-range XY order* or *off-diagonal long-range order* (LRO) [37]. Such LRO is the defining feature of continuous symmetry breaking in finite quantum systems.

Rather than the long-distance plateau, an equally good order parameter for $U(1)$ symmetry breaking is given by the in-plane magnetization squared

$$m_{\text{FM/AFM}}^2 = \frac{1}{N^2} \sum_{i, j} (\pm 1)^{(r_i^x + r_j^x)/a} C^x(i, j) \quad (10)$$

where a is the lattice spacing, and the sign is taken $+1$ for m_{FM}^2 , and -1 for m_{AFM}^2 . In the $N \rightarrow \infty$ limit, any state with a correlation plateau $C_\infty^x \neq 0$ will also have a finite magnetization $m_{\text{FM/AFM}}^2$, and vice versa [50].

When continuous symmetry breaking occurs in the thermodynamic limit, then at finite size the lowest energy state in

each S^z sector will be approximately,

$$|\Gamma_s^{\text{FM/AFM}}\rangle = \frac{1}{\mathcal{N}_s} \int_0^{2\pi} \frac{d\theta}{2\pi} e^{is\theta} |\theta^{\text{FM/AFM}}\rangle \quad (11)$$

where $|\theta^{\text{FM/AFM}}\rangle$ is the classical, symmetry-breaking product state where each spin points at angle θ or $-\theta$ in the xy -plane, s is an integer specifying the S^z sector, and \mathcal{N}_s is a normalization factor. Known either as the Anderson tower or Dicke states, $|\Gamma_s\rangle$ are angular momentum eigenstates of an emergent rigid rotor degree of freedom describing the collective orientation of all the spins in the system [48–51]. The true ground states in each S^z sector are also dressed by quantum spin wave fluctuations, which weaken the magnetic order [48]. For the ideal case of a uniform superposition over fully spin-polarized states $|\theta^{\text{FM/AFM}}\rangle$, the correlations in $|\Gamma_0\rangle$ lead to $C_\infty^x = m^2 = 0.5$, plus $1/N$ corrections. The effective in-plane magnetization of a $U(1)$ -symmetric state should thus be identified as $m_{\text{eff}} \equiv \sqrt{2C_\infty^x}$. That is, if one were to add a small symmetry-breaking field, then the corresponding non-symmetric ground state would have an average magnetization $\langle\sigma^x\rangle = m_{\text{eff}}$.

2. DMRG calculations

For a numerical investigation of the ground states, we apply the density matrix renormalization group (DMRG) algorithm [46]. We employ the general matrix product state (MPS) framework implemented in the TeNPy software library [47]. While MPS are best-representative of one-dimensional quantum systems, it is now routine to apply DMRG to two-dimensional models under certain geometric restrictions [58]. We always work with charge-conserving tensors that respect the $U(1)$ symmetry of the Hamiltonian.

To begin, we use DMRG to compute the ground state of H_{XY} and H_{nn} on $L \times L$ square clusters with open boundary conditions, for $L = 4, 6, 8$, and 10 . With all-to-all interactions included, we reliably obtain well-converged states at relatively low MPS bond dimensions, χ , as quantified by the truncation error of the discarded Schmidt states, ϵ_{trunc} . The most difficult finite system we study is $H_{\text{XY}}^{\text{AFM}}$ on the 10×10 lattice, for which $\epsilon_{\text{trunc}} < 10^{-5}$ at $\chi = 2048$. All other cases achieve the same or better convergence by $\chi = 1024$, or even $\chi < 200$ on the smaller systems.

All DMRG ground states feature the strong $\langle\sigma^x\sigma^x\rangle$ correlations expected in an XY LRO state. In Fig. 8a, we show the real-space correlation profile $C^x(d)$, which averages $C^x(i, j) = \langle\sigma_i^x\sigma_j^x\rangle$ over all spins i, j separated by a displacement vector \vec{d}_{ij} with length d . The long-range-interacting ferromagnet, $H_{\text{XY}}^{\text{FM}}$, exhibits a clear plateau in $C^x(d)$ at long distances for all system sizes. Such a plateau is less apparent for $H_{\text{XY}}^{\text{AFM}}$ and H_{nn} , although for either model $C^x(d)$ is still quite large at the longest distances. Furthermore, $C^x(d)$ increases with L in both models, suggesting the spatial decay of $C^x(d)$ is amplified by finite-size effects.

We also look for a finite squared magnetization, $m_{\text{FM/AFM}}^2$. We plot the finite-size dependence of this quantity in Fig. 8b,

which is consistent with $m_{\text{FM/AFM}}^2 > 0$ as $L \rightarrow \infty$. To further test the effects of the long-range interactions, we introduce a cutoff radius R_{max} , and only include interactions between spins i, j separated by distance $d_{ij} < R_{\text{max}}$. We find that ground state properties converge quickly with respect to this approximation parameter; the long-range interactions do not induce a quantum phase transition in either model. In Fig. 8c, we show the dependence of $m_{\text{FM/AFM}}^2$ on R_{max} , finding that, at fixed system size, it is not strongly dependent on $R_{\text{max}} > 4$. This is not too surprising: with the moderately fast $1/r^3$ decay, the interaction strength beyond this point is on the order of $0.01 J$ or less.

Overall, $H_{\text{XY}}^{\text{FM}}$ is clearly XY LRO, while $H_{\text{XY}}^{\text{AFM}}$ and H_{nn} exhibit stronger finite-size effects. Given that H_{nn} is rigorously known to be LRO in the thermodynamic limit, the similar behavior observed for $H_{\text{XY}}^{\text{AFM}}$ is a strong indication that it is as well.

3. Quantum phase diagram of $H_{\text{XY}} + H_Z$

We now investigate the ground state phase diagram in the presence of the externally applied light-shift δ , described by H_Z (Eq. 6). This perturbation preserves the $U(1)$ symmetry of H_{XY} , as well as the anti-unitary time-reversal symmetry. On the other hand, H_Z breaks the Ising symmetry $\sigma_i^z \rightarrow -\sigma_i^z$, and reduces the spatial rotation and translation symmetries. For sufficiently large δ , the lowest energy state of $H_{\text{XY}} + H_Z$ has $M^z \neq 0$, but such states are dynamically decoupled from the $S^z = 0$ sector in which the adiabatic preparation protocol takes place. Henceforth, we always consider the ground states within the $S^z = 0$ sector, as these are the ones most relevant to the experiment.

Because the perturbation H_Z is $U(1)$ symmetric, the XY LRO phase of H_{XY} may be stable to a sufficiently small staggered field. Microscopically, the dominant effect of a small δ should be to slightly cant the spins towards the z -axis. This will in turn modify the spin stiffness and the spin wave velocity, but not destroy the underlying order. By contrast, when δ is very large, the ground state must be a gapped, trivial paramagnet, in which $\langle\sigma^x\sigma^x\rangle$ correlations decay to zero at long distances [59]. Between these two limits, we expect a quantum phase transition (QPT) at some critical value, δ_c , of the applied field. In a companion paper [57], we investigate this QPT in detail, finding that, in the thermodynamic limit, it is likely a continuous, second-order transition. For $H_{\text{nn}} + H_Z$, the transition is in the 3D XY universality class. For the $1/r^3$ models, the standard theory expectation is that the AFM QPT is in the same universality class as the short-range model (i.e. 3D XY), while the FM QPT is in a different universality class with mean-field-like critical exponents [15].

Here, we focus our attention on the 6×7 and 10×10 arrays studied in the experiment. We calculate the $S^z = 0$ ground state of $H_{\text{XY}} + H_Z$ at various light-shifts δ using DMRG. At these system sizes, the sharp QPT expected in the thermodynamic limit is smoothed to a broad crossover between the XY-ordered phase for small δ , and a trivial paramagnet for large δ . Three features of this crossover are shown in Fig. 8d-f.

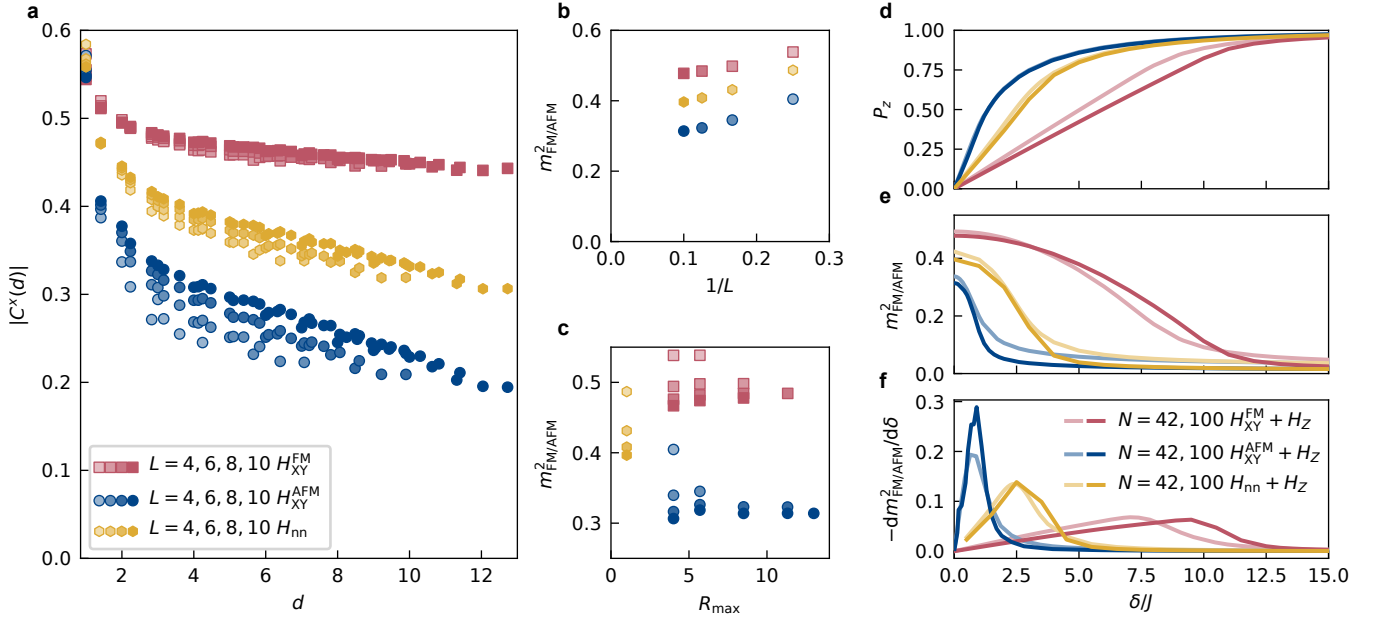


Figure 8. **DMRG ground state calculations.** **a**, Real-space correlation profile $|C^x(d)|$ on $L \times L$ square clusters with open boundary conditions. The ground state of H_{XY}^{FM} clearly exhibits XY LRO at all system sizes. For H_{XY}^{AFM} and H_{nn} , the correlations decrease at long distances, but this decay is reduced as L increases. **b**, Finite-size scaling of the magnetization $m_{\text{FM/AFM}}^2$. All three models are consistent with $m_{\text{FM/AFM}}^2 > 0$ as $L \rightarrow \infty$. **c**, Dependence of $m_{\text{FM/AFM}}^2$ on the interaction distance cutoff R_{max} . At each system size, the ground state correlations are well-converged by $R_{\text{max}} \approx 4$. **d-f**, Ground state properties of $H_{XY} + H_Z$ as a function of δ . There is a smooth crossover from the XY ordered state at $\delta = 0$ to the staggered paramagnet as $\delta \rightarrow \infty$. The $-dm^2/d\delta$ peaks (**f**) are finite-size incarnations of the quantum phase transition expected in the thermodynamic limit; we use their centers to define the crossover point $\hbar\delta_c/J$.

First, in Fig. 8d, we plot the staggered σ^z polarization,

$$P_z = \frac{1}{N} \sum_{i \in A} \langle \sigma_i^z \rangle - \frac{1}{N} \sum_{i \in B} \langle \sigma_i^z \rangle \quad (12)$$

which measures the alignment with the staggered field H_Z . For large $\delta \gg \delta_c$, the ground state approaches the staggered product state used to initialize the adiabatic ramp in the experiment, and the polarization saturates to $P_z = 1$. For $\delta = 0$, $P_z = 0$ due to the Ising symmetry of H_{XY} , which enforces $\langle \sigma_i^z \rangle = 0$. We emphasize that $P_z = 0$ is *not* a generic feature of the XY-ordered phase. Indeed, for small $\delta < \delta_c$, the spins partially align with the applied field, yielding $P_z > 0$.

Figure 8e displays the complementary behavior for the magnetization, $m_{\text{FM/AFM}}^2$. At small δ , the field-induced canting of the spins towards the z -axis causes $m_{\text{FM/AFM}}^2$ to decrease proportionally to δ^2 . At large δ , the ground state approaches the (staggered) z -aligned product state, in which $m_{\text{FM/AFM}}^2 = 0$. The magnetization changes most rapidly at the crossover, giving rise to the clear peaks in $dm_{\text{FM/AFM}}^2/d\delta$ shown in Fig. 8f. We take the center of these peaks as our definition of the crossover point, $\delta_c^{\text{FM/AFM}}$. For the $N = 42$ cluster, the values are $\hbar\delta_c^{\text{FM}}/J = 7.1(3)$, $\hbar\delta_c^{\text{AFM}}/J = 0.8(1)$, and $\hbar\delta_c^{\text{nn}}/J = 2.4(1)$. For the $N = 100$ cluster, we find $\hbar\delta_c^{\text{FM}}/J = 9.5(3)$, $\hbar\delta_c^{\text{AFM}}/J = 0.9(1)$, and $\hbar\delta_c^{\text{nn}}/J = 2.5(9)$. As $N \rightarrow \infty$, the smooth crossover is expected to sharpen into a *bona fide* QPT, and $m_{\text{FM/AFM}}^2(\delta)$ will be non-analytic at the critical point.

D. Adiabatic preparation - theory and numerics

We now provide theoretical and numerical analyses of the adiabatic preparation protocol used in the experiment. As mentioned above, we study both the FM and AFM cases considering $H_{XY}^{\text{AFM}} = -H_{XY}^{\text{FM}}$. Additionally, for a time-reversal-symmetric Hamiltonian such as $H = H_{XY} + H_Z$, the dynamics under $H(t)$ and $-H(t)$ are identical (as long as the initial state is also time-reversal-symmetric) [44]. So for a finite-time (quasi-adiabatic) ramp, the diabatic errors incurred attempting to follow the topmost state of $H_{XY}^{\text{FM}} + H_Z$ are the same as for a ground-state protocol with $H(t) = H_{XY}^{\text{AFM}} - H_Z(t)$.

1. Excitation gaps and an alternative protocol

The success of any finite-duration adiabatic protocol depends crucially on the low-energy spectrum of the system. In particular, as the smallest excitation gap encountered along the chosen path through parameter space decreases, the time required to obtain a final, high-fidelity ground state increases. To this end, we computed the minimal energy gaps, Δ_{min} , using exact diagonalization on finite clusters with periodic boundary conditions.

In Fig. 9a, we plot the instantaneous gap Δ_{min} of $H_{XY}^{\text{FM/AFM}} + H_Z$, in the $S^z = 0$ sector, as a function of the light-shift $\hbar\delta/J$. We expect the gap for either case to be small-

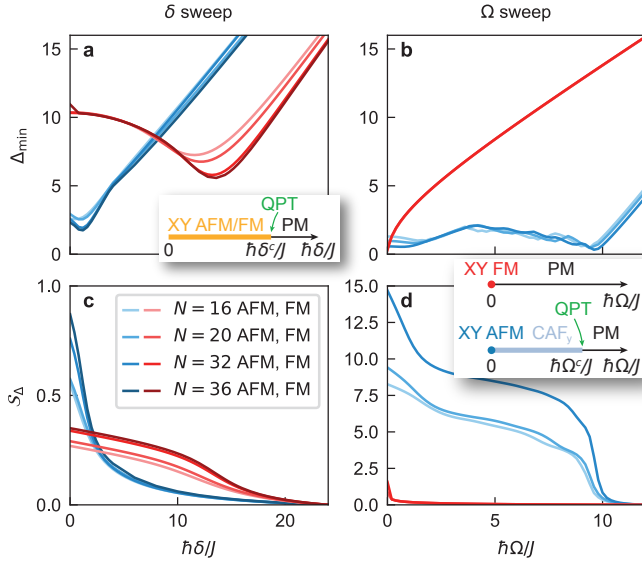


Figure 9. **Excitation gap for two adiabatic preparation protocols.**

a. Minimal energy gaps of $H_{XY}^{\text{AFM(FM)}} + H_Z$ to the lowest excited state in the $M^z = 0$ sector as a function of $h\delta/J$. We here only consider gaps among states with momentum $\vec{k} = 0$ and fully symmetric under the lattice point-group, which reflects the setup in the (ideal) experiment. Blue (red) curves show the results for the AFM (FM) model. Darker colors correspond to larger system sizes. The inset shows a sketch of the expected phase diagram. **b.** Same as **a**, but for the protocol with Hamiltonian $H_{XY}^{\text{AFM(FM)}} + H_X$. Here we cannot restrict the analysis to a single M^z sector since it is not conserved. **c.** Cumulatively integrated $1/\Delta_{\min}^2$ [starting from the largest value $h\delta/J = 24$] for the gaps shown in **a**. The values at $h\delta/J = 0$ measure how difficult it is to prepare the ground state of $H_{XY}^{\text{AFM(FM)}}$ by sweeping δ . **d.** Same as **c** but for the gaps along Ω , as shown in **b**. The inset shows a sketch of the expected phase diagrams for $H_{XY}^{\text{AFM(FM)}} + H_X$.

est near the quantum phase transition (Methods C3): for the FM, this dip is seen at $h\delta/J \approx 12$, while in the AFM the gap is minimal when $h\delta/J \lesssim 2$. The size of the minimal gaps decreases with increasing system size N (darker colors), as one would expect at a QPT. However, we find the minimal finite-size gaps for the FM model are always larger than the ones for the AFM model. This indicates that for the dipolar XY model, the FM requires less total ramp time to prepare than the AFM.

Besides the staggered light-shift ramp demonstrated in the main text, one can conceive a different route for preparing XY-ordered states: tune down a spatially *uniform* field in the x direction from large values $h\Omega \gg J$ to zero. This is similar to what is done in Rydberg quantum simulations of the two-dimensional Ising model [8, 9, 60], and was used in a prior experiment to prepare the topological ground state of a one-dimensional XY model [61]. The corresponding Hamiltonian is $H_{XY}^{\text{AFM(FM)}} + H_X(t)$, with $H_X(t) = \hbar\Omega(t) \sum_i \sigma_i^x/2$. Note that M^z is no longer conserved in the presence of H_X .

Figure 9b shows the smallest energy gap for this alternative protocol. The behaviour is very different from the one for the δ sweep discussed above. For FM interactions, the

gap does not show any local minimum and remains large until the end of the sweep, where it finally narrows. By contrast, the gap for the XY AFM is small in the whole region $h\Omega/J \lesssim 10$. Based on previous studies of the nearest-neighbor XY model [62, 63], both of these results are likely a consequence of the expected phase diagram for $H_{XY}^{\text{FM/AFM}} + H_X$, which we sketch in the inset of Fig. 9d. For the XY FM, H_X is a relevant perturbation to the ordered phase: any non-zero Ω breaks the $U(1)$ symmetry and, in the thermodynamic limit, immediately destroys the LRO, resulting in a paramagnetic (PM) phase. The AFM is also XY-ordered only at the $U(1)$ -symmetric point $\Omega = 0$, but a small Ω instead “cants” the AFM order towards the y -direction by a spin-flop process [62, 63]. The ground state is then still an antiferromagnet, but one ordered along the y -direction, i.e. it spontaneously breaks the remaining \mathbb{Z}_2 symmetry $\sigma^y \rightarrow -\sigma^y$ of $H_{XY} + H_X$. This “canted” antiferromagnet (CAF_y) is stable up to a critical value $h\Omega_c/J$ where it finally undergoes a 2 + 1D Ising QPT to the PM phase [63].

Comparing the gap landscapes in Fig. 9a,b suggests that preparing the XY AFM requires less time when using δ sweeps instead of the Ω sweeps. To quantify this, we integrate the squared inverse gaps and define

$$\mathcal{S}_\Delta(\lambda) = \int_{\lambda_0}^{\lambda} \frac{1}{\Delta_{\min}(\lambda')^2} d\lambda' \quad (13)$$

where $\lambda = h\delta/J$ or $h\Omega/J$ is the dimensionless parameter for either protocol. As one motivation for this quantity, we consider the fidelity susceptibility, χ_F , which is the leading term in the expansion of the fidelity $F(\lambda, \lambda + \delta\lambda) = |\langle \psi_0(\lambda) | \psi_0(\lambda + \delta\lambda) \rangle|$ of the ground states $|\psi_0(\lambda)\rangle$ between two close points λ and $\lambda + \delta\lambda$ in parameter space [64],

$$F(\lambda + \delta\lambda) = 1 - \frac{\delta\lambda^2}{2} \chi_F + \dots \quad (14)$$

The coefficient χ_F characterizes how quickly the ground state changes with λ . For a ramp protocol of the form $H(\lambda) = H_{XY} + \lambda H_I$, one can show

$$\chi_F = \sum_{n \neq 0} \frac{|\langle \psi_n(\lambda) | H_I | \psi_0(\lambda) \rangle|^2}{(E_n(\lambda) - E_0(\lambda))^2} \quad (15)$$

where $|\psi_n(\lambda)\rangle$ is the n -th eigenstate of $H(\lambda)$ and $E_n(\lambda)$ is the corresponding energy [64]. If we assume that the $n = 1$ term is dominant, and the numerator is nearly constant, we get the relationship $\chi_F \sim 1/(E_1(\lambda) - E_0(\lambda))^2 = 1/\Delta_{\min}(\lambda)^2$. The integral \mathcal{S}_Δ therefore estimates the total difficulty of adiabatically preparing the ground state of $H(\lambda)$, starting from the ground state of $H(\lambda_0)$.

In Fig. 9c,d, we plot $\mathcal{S}_\Delta(\lambda)$ for the two protocols. The initial point λ_0 is taken to be in the paramagnetic phase: $\lambda_0 = 12$ for the δ sweep and $\lambda_0 = 24$ for the Ω sweep. In either case, \mathcal{S}_Δ for the AFM (blue curve) exceeds that of the FM as $\lambda \rightarrow 0$, indicating that the AFM is more difficult to prepare. Most importantly, comparing Fig. 9c,d, one sees that the $H_Z(t)$ protocol is much more efficient at preparing the XY ordered state ($\lambda = 0$) than the $H_X(t)$ protocol, especially for the AFM.

2. Time-dependent MPO-MPS simulation

To ensure that we have a good understanding of the experiment and its imperfections, we also perform numerical simulations of the full many-body quantum dynamics for the $N = 42$ adiabatic ramp. We simulate the dynamics in the spin-1/2 subspace, taking into account the error tree in Fig. 6 by sampling the state preparation errors with $N_{\text{dis}} = 20$ independent simulations.

Atoms that were not excited in the STIRAP with $\eta_{\text{STIRAP}} = 0.03$ correspond to missing sites in the square lattice not taking part in the dynamics. On the remaining sites, we prepare an initial MPS as product state, flipping individual spins according to the probabilities of the microwave π -pulse, $\eta_{\text{MW}} = 0.003$, and the subsequent microwave sweep of the addressed atoms, $\eta_{\text{A}} = 0.10$, $\eta_{\text{B}} = 0.03$. These values are slightly different from those reported in Table I, reflecting an earlier calibration of the experiment. We further update the atom distances r_{ij} in H_{XY} to account for positional disorder: we first take a normal-distributed initial displacement from the square lattice with variance $\sigma_r = 0.2 \mu\text{m}$, followed by a movement during the dynamics with normal-distributed (time-independent) velocity of variance $\sigma_v = 0.05 \mu\text{m}/\mu\text{s}$ corresponding to the temperature of the atoms.

We then time-evolve the states under the time-dependent Hamiltonian,

$$H(t) = -J \sum_{i < j} \frac{a^3}{r_{ij}^3(t)} [S_i^+ S_j^- + S_i^- S_j^+] + H_{\text{vdW}} + \delta(t) \epsilon_{\text{AFM}} \sum_{i \in B} \frac{1 + \sigma_i^z}{2} \quad (16)$$

where $J/h = 0.77 \text{ MHz}$, $\delta(t)$ is the ramp shown in Fig. 10a,c (insets), and $\epsilon_{\text{AFM}} = -1$ for the antiferromagnet (+1 for the ferromagnet). The additional term, H_{vdW} , accounts for the van der Waals interactions between the Rydberg atoms, and takes the form

$$H_{\text{vdW}} = \sum_{i < j} \frac{a^6}{r_{ij}^6(t)} [U_6^{PP} P_i^\uparrow P_j^\uparrow + U_6^{SS} P_i^\downarrow P_j^\downarrow + U_6^{SP} (P_i^\uparrow P_j^\downarrow + P_i^\downarrow P_j^\uparrow)] \quad (17)$$

where $P_i^{\uparrow/\downarrow} = S_i^z \pm 1/2$ are single-spin projectors. The values of the U_6 coefficients are $U_6^{PP}/h = -0.008 \text{ MHz}$, $U_6^{SS}/h = 0.037 \text{ MHz}$, and $U_6^{SP}/h = -0.0007 \text{ MHz}$. For the purposes of this simulation, we restrict the interaction range of H_{XY} and H_{vdW} to $R_{\text{max}} < 3.7$. We use the W_{II} method [65] to approximate the evolution operator $e^{-i(H/h)dt}$ as a matrix product operator (MPO), in combination with standard variational MPO-MPS compression methods. Our scheme is correct to first order in the time step $dt = 0.01 \mu\text{s}/2\pi$. Since the evolution is sufficiently adiabatic, a moderate bond dimension of $\chi = 128$ is enough to capture the correlations. In the DMRG ground state, the truncation error at this bond dimension is 6×10^{-7} for the ferromagnet, and 3×10^{-5} for the antiferromagnet.

When evaluating expectation values and correlation functions from the time-evolved MPS (t -MPS), we further account for the measurement errors $\eta_{\text{frz}} = 0.01$, $\eta_{\text{dx}} = 0.03$, $\epsilon = 0.01$, $\epsilon' = 0.07$ of the error tree. This can be done exactly (without another sampling procedure), since the MPS gives full access to the probabilities of the individual measurement outcomes.

There are two notable experimental imperfections that we do not take into account in these simulations. First, there are further sources of decoherence in the experiment as discussed in B 2. Second, in our numerical simulations, we assume that all errors in the error tree occur independently for each atom and result in an initial product state of up or down spins or vacant holes. Yet, the STIRAP and microwave pulses leave the atoms in coherent superpositions of the relevant atom levels.

3. Simulation results for $N = 42$

The results of the t -MPS simulations are shown in Fig. 10, which also includes direct comparisons to the experimental measurements, and to the DMRG ground state. For our ensemble of $N_{\text{dis}} = 20$ independent t -MPS simulations, we show the average values of these simulations with solid lines, while the shaded region indicates the standard deviation.

Our first observable (Fig. 10a,c) is the staggered polarization $P_z = \sum (\pm)_{A,B} \langle \sigma_i^z \rangle$. For the antiferromagnet, the agreement between the t -MPS simulations and experiment is essentially perfect for all values of δ . This is a strong indication that most dominant sources of error in the experiment have been accurately accounted for. For the ferromagnet, there is a small offset between the t -MPS calculation and the experimental result at late times (small δ). In particular, $P_z \rightarrow 0$ as $\delta \rightarrow 0$ for the t -MPS calculation, while $P_z \rightarrow -0.06$ in the experiment. This discrepancy is due to the sublattice-dependent depumping from the light-shift discussed in Sec. B 2, which we do not account for in the t -MPS simulations.

As the state loses its initial σ^z polarization, it concomitantly develops XY order. This is tracked by the order parameter m_{FM}^2 (m_{AFM}^2 for the antiferromagnet), shown in Fig. 10b,d. We obtain again a good agreement between the t -MPS simulation and the experiment at early times (large δ), although we caution that the initial positive value of $m_{\text{FM/AFM}}^2 = 1/42$ is inherent to any σ_i^z -product state. On top of the smooth adiabatic envelope, the t -MPS simulations reveal coherent oscillations in P^z and $m_{\text{FM/AFM}}^2$. These oscillations are a feature of the large- δ paramagnetic phase, and are essentially Rabi oscillations between the classical Néel ground state and the 42-fold degenerate manifold of states with one spin-flip excitation.

At small δ , the experimental measurements of $m_{\text{FM/AFM}}^2$ fall below the t -MPS predictions. This deficit likely arises from a combination of decoherence and unmodeled systematic errors, such as experimental imperfections in the $\pi/2$ -pulse rotation to the x basis. Regarding the latter, an imperfect basis rotation means that the operator measured in the experiment is not exactly σ_i^x but some small modification of it, $\tilde{\sigma}_i^x = U \sigma_i^x U^\dagger$. In XY-ordered states, $\langle \sigma^x \sigma^x \rangle = \langle \sigma^y \sigma^y \rangle$ correlations are typically much larger than any other two-body

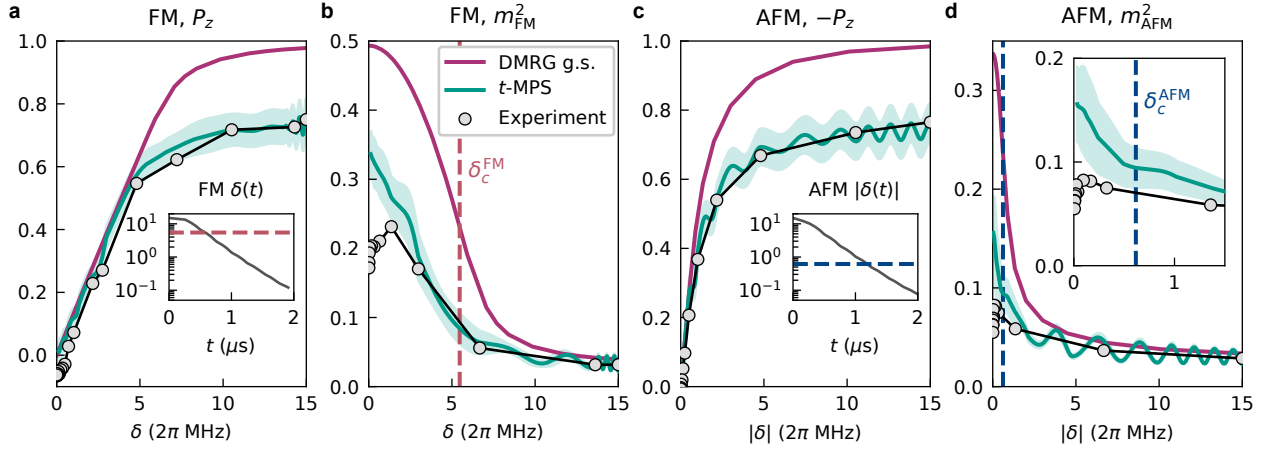


Figure 10. **Numerical simulation of the adiabatic preparation for the 6×7 lattice.** We compare the predictions from the t -MPS simulations (disorder ensemble average in dark teal, standard deviation in light teal) to the experimental data (gray), as measured at light-shift $\delta(t) = \delta$. We also show the ground-state expectation value from DMRG (purple) **a**, The staggered polarization P_z of the FM. Theory and experiment agree remarkably well, except for an offset at small δ , due to the light-shift-induced depumping. Inset: ramp $\delta(t)$ used for the FM simulation. **b**, The ferromagnetic magnetization $m_{\text{FM}}^2(\delta)$. We find excellent agreement between experiment and numerics for $\delta > 2$, including near the phase transition at $\delta_c^{\text{FM}} = 5.5$ (red dashed line). The two diverge somewhat at smaller δ (later times), likely due to decoherence and unmodeled systematic measurement errors. **c**, **d**, Corresponding results for the AFM. For P_z , the t -MPS simulation accurately reproduces the experimental data across the whole $\delta(t)$ sweep. For δ far above $\delta_c^{\text{AFM}} = 0.6$ (blue dashed line), there are many-body Rabi oscillations characteristic of the paramagnetic phase. **c**, Inset: ramp $\delta(t)$ used for the AFM simulation. **d**, Inset: zoom-in of lower left corner. At small δ (late times), the magnetization m_{AFM}^2 measured in experiment is below that predicted from the simulations.

operators, especially at long distances. Measuring any modified $\tilde{\sigma}_i^x$ will then generically reduce the value of the inferred magnetization, $\tilde{m}_{\text{FM}}^2 = 2 \sum_{i,j} \langle \tilde{\sigma}_i^x \tilde{\sigma}_j^x \rangle$.

We also use the t -MPS simulation to assess the quality of the adiabatic preparation. In particular, we are interested in how close the unitary dynamics comes to preparing the target ground state of H_{XY} . We measure this via the XY energy $E_{\text{XY}} = \langle H_{\text{XY}} \rangle$, which corresponds to the amount of energy the many-body state stores within the dipolar interaction. The ideal endpoint of the ramp is a state that maximizes $|E_{\text{XY}}|$, i.e. the ground state of H_{XY} (or, the topmost state in the case of the negative-temperature preparation for the antiferromagnet). We do not include measurement errors for this analysis, as we want to directly compare the adiabatically prepared state to the ideal one. As a minor technical point, the ensemble of lattices used in the t -MPS simulation occasionally have missing sites (representing an absence of Rydberg-excited atoms), and always have some position disorder which modifies the couplings, Ja^3/r_{ij}^3 , and hence the spectrum of H_{XY} . To treat the different lattices on even footing, when measuring E_{XY} we compute the expectation value of H_{XY} without position disorder in the couplings, and normalize by the total number of active sites, \bar{N} , before taking the ensemble average.

Figures 11a,b show $E_{\text{XY}}(\delta)/J\bar{N}$ in the DMRG ground state (purple), the ensemble-averaged t -MPS simulation (teal), and a single state within the t -MPS ensemble (pink) that had a nearly perfect initial configuration: one missing site at the corner, and all remaining spins properly aligned with the staggered field. Initially, the system is in a classical ensemble of σ_i^z -aligned product states, so $E_{\text{XY}}(t=0) = 0$. The dynamics generated by $H(t)$ produce the desired corre-

lations among the spins; the oscillations in E_{XY} at large δ are the paramagnetic Rabi oscillations also observed in P_z and m_x^2 . At the end of the ramp, the ensemble averages are $E_{\text{XY}}^{\text{FM}}/(\bar{N}J) = -1.41(8)$ and $E_{\text{XY}}^{\text{AFM}}/(\bar{N}J) = -0.64(3)$, which respectively correspond to $94 \pm 5\%$ and $89 \pm 4\%$ of the $N = 42$ ground state value. Remarkably, the near-ideal initial state produces a near-ideal final state, achieving 99.7% (FM) and 98.2% (AFM) of the ground state energy density. This indicates that any diabatic errors during the ramp are negligible compared to the initialization errors.

As discussed in Sec. D 1, the quality of a finite-time adiabatic ramp crucially depends on the size of the many-body energy gap. For the $U(1)$ -symmetric ramp at hand, the quantity is the (spin-)neutral gap, $\Delta_0 = E_1(S^z = 0) - E_0(S^z = 0)$. In the paramagnetic phase, $\Delta_0 \sim \delta$, while in the XY-ordered phase one expects $\Delta_0^{\text{FM}} \sim 1/\sqrt{N}$ and $\Delta_0^{\text{AFM}} \sim 1/N$ [18, 27]. The numerical value of Δ_0 on finite-size systems can be computed in DMRG by solving for the lowest-energy state orthogonal to the previously obtained ground state, in the same $S^z = 0$ sector. We plot $\Delta_0(\delta)$ in Fig. 11c,d for both the $N = 42$ and $N = 100$ clusters. The behavior of $\Delta_0(\delta)$ differs somewhat from that seen in Sec. D 1, due to a difference in boundary conditions (open instead of periodic). Across the phase diagram, $\Delta_0(\delta)$ is fairly large, which helps to explain the success of the adiabatic preparation: the ramp decay time scale, $\tau = 1.45 \hbar/J$, is slower than (FM) or approximately equal to (AFM) the inverse gap, $\Delta_0^{-1} = 0.45/J$ (FM), $1.47/J$ (AFM). The smaller gap for the antiferromagnet is a manifestation of its frustration, and makes adiabatically preparing its ground state more difficult compared to $H_{\text{XY}}^{\text{FM}}$. Comparing Δ_0 to the excess energy the end of the

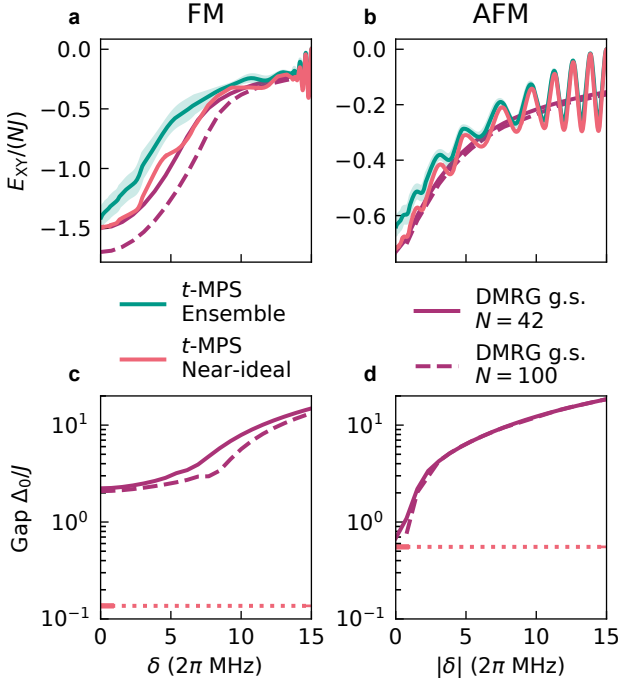


Figure 11. **Energetics of the simulated adiabatic preparation.** **a, b,** Interaction energy density $E_{XY}/\bar{N}(\delta)$ in the t -MPS simulations of the 6×7 lattice. The teal line and envelope are the disorder ensemble average and standard deviation, respectively. Following a single state with minimal initialization errors (pink line), we see that E_{XY} tightly follows the DMRG ground state value (purple), confirming that diabatic errors are negligible. **c, d,** Energy gaps Δ_0 between the ground state and the first excited state in the $S^z = 0$ sector, obtained from DMRG. For the near-ideal initial state, the final energy density (pink dotted line) falls below the gap in both the FM and AFM case.

ramp, we find that the near-ideal initial state ends up with a total effective energy, $\mathcal{E} = NE_{XY}/\bar{N}$, below the many-body gap. The difference is remarkably large for the ferromagnet ($\mathcal{E}/\Delta_0^{\text{FM}} = 0.06$), implying a near-flawless adiabatic sweep, while the margin for the antiferromagnet is much narrower ($\mathcal{E}/\Delta_0^{\text{AFM}} = 0.81$).

E. Thermal phase diagram

We conclude by discussing the phase diagram of $H_{XY} + H_Z$ at finite temperature, T (measured in unit of k_B). While two-dimensional, $U(1)$ -symmetric systems can have XY LRO ground states, for short-range interacting models such as H_{nn} this order does not persist to finite temperature [12, 13, 66, 67]. Physically, this is because spin-wave excitations (i.e. Goldstone modes) proliferate at finite temperature and destroy the XY order. Instead, most two-dimensional XY models have an *algebraic long-range ordered* phase at low temperatures, separated from the high- T disordered phase by a Berezinskii-Kosterlitz-Thouless (BKT) transition at a critical temperature T_{BKT} [38–41]. The low- T phase is characterized by power-law-decaying correlations, $C^x(d) \sim d^{-1/(2\pi K)}$, with a temperature-dependent exponent K that attains the uni-

versal value $K_{\text{BKT}} = 2/\pi$ at T_{BKT} . For the classical nearest-neighbor XY model, $T_{\text{BKT}}^{\text{cl}}/(2J) = 0.892943(2)$ [68, 69], while in the quantum spin-1/2 H_{nn} the transition is lowered to $T_{\text{BKT}}^{\text{nn}}/(2J) = 0.353(3)$ [70, 71].

Long-range ferromagnetic interactions can suppress the proliferation of spin-waves and thus renew the possibility for XY LRO at finite temperature [18, 19, 27]. With $1/r^\alpha$ ferromagnetic couplings, extensively large fluctuations of the spin orientation come at an energy cost proportional to $L^{4-\alpha}$, with L the linear system size, so two-dimensional XY LRO can be thermodynamically stable when $\alpha \leq 4$. Indeed, in 1976, Kunz and Pfister proved that the classical version of H_{XY}^{FM} exhibits a finite-temperature phase transition between the high- T disordered phase and a low- T XY LRO phase [17]. Subsequent Monte Carlo simulations located this transition at $T_c^{\text{FM}}/(2J) = 3.96(4)$, and suggested it was weakly first-order [72, 73]. We note this is contrary to the general expectation of a second-order symmetry-breaking transition, in a mean-field-like universality class when $\alpha \leq 3$ [15, 74, 75]. Finally, $1/r^\alpha$ antiferromagnetic interactions do not essentially modify the energy of long-wavelength fluctuations, so one expects the low- T physics of H_{XY}^{AFM} to be similar to that of H_{nn} [14].

1. Numerical phase diagram for $N = 42$

For a quantitative understanding of the thermal physics accessible in the experiment, we numerically investigate the finite temperature phase diagram for both the FM and the AFM on the 6×7 lattice. While H_{XY}^{FM} is amenable to Quantum Monte Carlo techniques, these are not an option for H_{XY}^{AFM} , which exhibits a sign problem. Instead, for both we employ the Minimally Entangled Typical Thermal States (METTS) algorithm [76]. This is a Markov chain Monte Carlo (MCMC) approach that alternates between evolving a state in imaginary time to inverse temperature $\beta/2$, and then taking a projective measurement as the initialization for the next imaginary time evolution. The result is an ensemble of pure states, $\{|\psi_{\text{METTS}}\rangle\}$, that approximates the thermal density matrix $\rho \propto e^{-\beta H}$: for any operator \mathcal{O} , the ensemble average of $\langle \psi_{\text{METTS}} | \mathcal{O} | \psi_{\text{METTS}} \rangle$ approaches the thermal equilibrium value $\text{Tr}[\rho \mathcal{O}]$.

Due to the $U(1)$ symmetry, the thermal density matrix factorizes into a direct sum over the different magnetization sectors, $\rho = \bigoplus_{m=-N}^N \rho_m$. Here, we sample only from the $m = 0$ sector, as this is the most relevant one for the partial quench experiment. For numerical convenience, we also truncate the long-range interactions to $R_{\text{max}} < 3.7$, and omit the van der Waals coupling, position disorder, and the possibility of holes. We perform the imaginary time evolution using the same W_{II} MPO-MPS method as in Sec. D 3, taking an MPS bond dimension of $\chi = 256$. We found very similar results using $\chi = 128$ (not shown), albeit with some small quantitative shifts near the finite-temperature phase transition. To reduce sample autocorrelations, each projective measurement is made in a random basis determined by a depth-two, $U(1)$ -conserving random unitary circuit [77]. By a standard

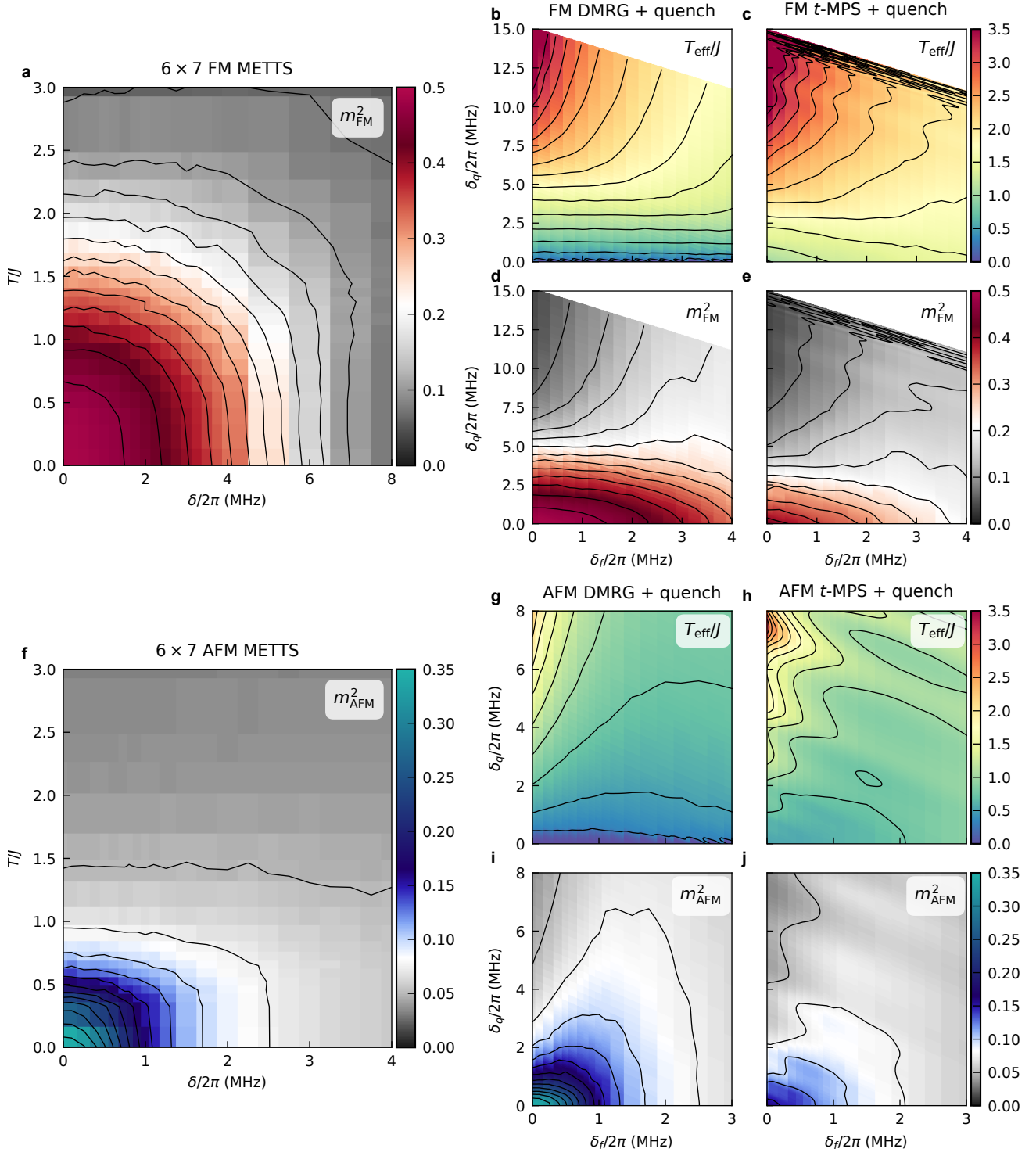


Figure 12. **Finite-temperature properties of $H_{XY} + H_Z$.** **a**, Phase diagram of $H_{XY}^{\text{FM}} + H_Z$ at finite temperature T and light-shift δ , computed from METTS on a 6×7 array in the $M^z = 0$ sector. We also include $T = 0$ points calculated from DMRG. The region with large magnetization m_{FM}^2 at small δ and small T should correspond to the LRO phase in the thermodynamic limit. The colorbar is chosen so that dark red corresponds to the final m_{FM}^2 calculated in the t -MPS simulation, absent measurement errors. Thin black lines are equal-magnitude contours to guide the eye. **b,c**, Estimated temperature of a quench experiment with final light-shift δ_f and quench magnitude δ_q , taking the pre-quench configuration to be either the DMRG ground state (**b**) or the t -MPS ramp simulation ensemble (**c**). The oscillatory behavior seen in **c** stems from the paramagnetic Rabi oscillations discussed in Sec. D 3. **d, e** Corresponding magnetization m_{FM}^2 of the system at temperature $T_{\text{eff}}(\delta_f, \delta_q)$. **f-j** Analogous results for the antiferromagnet. The region with finite magnetization m_{AFM}^2 is expected to become an algebraic-ordered (BKT) phase in the thermodynamic limit.

blocking analysis, we estimate the resulting autocorrelation time to be about 10 MCMC steps [78]. We therefore allow a warm-up time of 20 steps, and then generate 100-300 samples for each value of δ and β .

In Fig. 12a,f, we show 2D color plots of the squared magnetization $m_{\text{FM/AFM}}^2$ at finite T and δ . For the ferromagnet (Fig. 12a), we observe a lobe around $(T, \delta) = (0, 0)$ that corresponds to the XY-ordered phase. The order begins to disappear around $T/J = 1.5$ (for the thermal phase transition) and $\delta/J = 5$ (for the quantum phase transition). Examining m_{AFM}^2 for the AFM case (Fig. 12b), we observe a smaller lobe with apparent XY order. Although $H_{\text{XY}}^{\text{AFM}}$ is not predicted to host true long range order at $T > 0$, obtaining $m_{\text{AFM}}^2 > 0$ is still possible on finite-size systems.

Owing to the small system size, there is a smooth crossover between the ordered and disordered regimes for both models, and it is difficult to ascertain what the nature of the phase transition may be in the thermodynamic limit. It should be possible to study larger system sizes for $H_{\text{XY}}^{\text{FM}}$ using Quantum Monte Carlo methods [79], which is beyond the scope of this work. For now, we cautiously estimate $T_{\text{XY}}^{\text{FM}}/J \approx 1.5$ and $T_{\text{XY}}^{\text{AFM}}/J \approx 0.5$, as the $\delta = 0$ crossover temperature into the high- T phase. Compared to H_{nn} , for which $T_{\text{BKT}}^{\text{nn}}/J = 0.706(6)$ [70, 71], the dipolar ferromagnet appears to have a higher transition temperature (although not as high as the classical model [72, 73]), while the antiferromagnet may have a slightly lower one.

2. Temperature estimate of the final state

With our METTS representation of the thermal density matrix, we also determine the temperature and δ dependence of the internal energy, $E(T) = \text{Tr}[\rho H]$. The inverse function $T(E)$ defines a temperature calibration: we estimate the effective temperature of a state from its energy density. Inputting the mean final energy density of our t -MPS simulations (Sec. D), we estimate the effective temperatures at the end of the adiabatic ramp to be $T_{\text{MPS}}^{\text{FM}}/J = 0.95$ and $T_{\text{MPS}}^{\text{AFM}}/J = 0.53$. The t -MPS disorder ensemble results in a spread of energies $E_{\text{XY}} \pm \sigma_E$; the corresponding temperature intervals are $T_{\text{MPS}}^{\text{FM}} \in [0.46, 1.17]$ and $T_{\text{MPS}}^{\text{AFM}} \in [0.45, 0.60]$. These intervals are asymmetric about the mean value due to the nonlinearity of $T(E)$. The obtained $T_{\text{MPS}}^{\text{FM}}$ appears to be below the estimated crossover temperature $T_{\text{XY}}^{\text{FM}}$, while for the antiferromagnet $T_{\text{MPS}}^{\text{AFM}}$ is very close to the phase transition. This is consistent with the wide spread in magnetizations m_{AFM}^2 over the t -MPS ensemble, shown in Fig. 10d.

3. Temperature calibration of quantum quenches

Performing an analogous $T(E)$ calibration at finite δ , we also estimate the effective temperatures produced by the quantum quench experiments (main text Fig. 1c,e,f), with final light-shift δ_f and quench magnitude δ_q . We assume that, following the quench, the system equilibrates to a thermal state; extensively testing this assumption with numerical quench

simulations is challenging, but may be interesting to explore in the future. Barring the possibility of a nonthermal equilibrium, our basic expectation is that the quench affects the XY order by a mechanism not unlike a finite-temperature bath. In particular, the excess energy added into the system should excite the low-energy, symmetry-restoring spin waves [80]. If the resulting population density of spin waves at equilibrium is not too different from a true thermal distribution, then in the thermodynamic limit it will destabilize the XY AFM order but not the XY FM order at low temperature.

We first calculate the effective temperature assuming *perfect* adiabatic preparation up to the pre-quench point $\delta_f + \delta_q$, i.e. by evaluating the energy $\langle H_{\text{XY}} + H_{\text{Z}}(\delta_f) \rangle$ in the DMRG ground state of $H_{\text{XY}} + H_{\text{Z}}(\delta_f + \delta_q)$ and then converting it to a temperature. Figure 12b,g shows the effective temperature $T_{\text{eff}}(\delta_f, \delta_q)/J$ for the FM and the AFM. In the FM, modest quenches $\delta_q/2\pi < 4$ MHz uniformly increase the effective temperature as a function of δ_f over the range $\delta_f/2\pi \in [0, 3.5]$ MHz probed in the experiment. With larger quenches, the effective temperature increases rapidly for small values of δ_f and slows down at larger values of δ_f . In the AFM, the effective temperature produced by even small quenches δ_q has a strong dependence on δ_f , again being much more effective at raising the temperature as $\delta_f \rightarrow 0$ (i.e. the isotherms are steeply sloped at small δ_f). Figure 12d,i show the corresponding magnetization $m_{\text{FM/AFM}}^2$ expected at $T_{\text{eff}}(\delta_f, \delta_q)$. Notably, in the AFM the large variation in $T_{\text{eff}}(\delta_f)$ at a fixed δ_q leads to a “tilted Matterhorn” shape for the ordered region.

Finally, we estimate the effective temperature of the full experimental protocol by using the states produced in the t -MPS ramp simulation as the pre-quench configuration. We show $T_{\text{eff}}(\delta_f, \delta_q)/J$ for the FM and AFM in Fig. 12c,h. As a consequence of the paramagnetic Rabi oscillations discussed previously in Sec., D 3, T_{eff} is also oscillatory. For the FM, these oscillations only manifest at large δ_q (corresponding to pre-quench states taken very early in the ramp), while for the AFM they are relevant across the phase diagram. The latter behavior ultimately stems from the fact that $\delta_c^{\text{AFM}}/2\pi \approx 0.7$ MHz, so most pre-quench states are in the paramagnetic phase.

The corresponding magnetization $m_{\text{FM/AFM}}^2(T_{\text{eff}})$ is shown in Fig. 12e,j. Comparing to the experimental results in Fig. 1e,f, we see that some qualitative features are reproduced by this calculation, especially for the AFM. For instance, the sloped phased boundary seen in the experiment at small δ_f is due to the diagonal isotherms. The calculation seems to differ from the experiment in the region with large δ_f (i.e. $\delta_f/2\pi > 2(1)$ MHz for the FM (AFM)) and small δ_q . In particular, the order-disorder crossover appears to happen at larger δ_f than seen in the experiment, and the observed non-monotonic behavior of $m_{\text{FM/AFM}}^2(\delta_q)$ is also less apparent. These differences may come from the same unmodeled imperfections that led to a discrepancy in the absence of any quench (see Sec., D 3). Another possibility is that the thermal density matrix $\rho(T_{\text{eff}})$ in the $M^z = 0$ sector may be an inadequate approximation of the post-quench state, either due to nonthermal equilibration or neglected contributions from different magnetization sectors.